International Journal of Heat and Mass Transfer 252 (2025) 127472

Contents lists available at ScienceDirect

International Journal of Heat and Mass Transfer

journal homepage: www.elsevier.com/locate/ijhmt

Flow-boiling instabilities in high aspect-ratio rectangular minichannels under single-sided heating at different inclinations

Marius Vermaak [a], Jaco Dirker [a,*], Daniel Orejon [b], Khellil Sefiane [b]

[a] Mechanical and Aeronautical Engineering Department, University of Pretoria, Pretoria 0028, South Africa
[b] School of Engineering, Institute for Multiscale Thermofluids, University of Edinburgh, Edinburgh EH9 3FD, United Kingdom

ARTICLE INFO

Keywords:
Inclination
Pressure instability
Flow-boiling
Micro/mini channel
Flow instabilities
Heat transfer

ABSTRACT

Flow boiling can potentially enhance the heat transfer performance of cooling systems for industrial and everyday microelectronics. Flow instability is difficult to prevent, and its impact on heat transfer performance, whether beneficial or detrimental, is poorly defined, slowing its adoption. To better understand the phenomenon, experimental pressure instabilities were analysed during flow-boiling of Perfluorohexane (FC-72) in a high aspect ratio rectangular minichannel at different inclinations under one-sided heating conditions to simulate heating from microelectronics. The flow passage had a width to height aspect ratio of 10 (5 mm × 0.5 mm) and a hydraulic diameter of 909 μm. Inclination angles ranged from -20° (downward flow) to 0° (horizontal flow) and up to +90° (vertical upward flow), for mass fluxes of 10 kg/m^2•s, 20 kg/m^2•s and 40 kg/m^2•s at a fluid saturation temperature of 56.0 °C for a subcooling degree between 36.0 °C and 38.3 °C. Compared to in the absence of instabilities, it was found that instability-driven cooling improved heat transfer performance and decreased the heated surface temperature by up to 15.0 °C (in the case of 60° upward flow at a mass flux of 10 kg/m^2•s and heat flux of 11.3 kW/m^2). Observed instability types included major reverse flow (severe pressure-drop oscillation), minor reverse flow (mild pressure-drop oscillation) and two-phase mixing. Reverse flow and two-phase mixing instability maps were created, which show that an increase in mass flux decreased the intensity of the reverse flow from major to minor as less vapour was generated, contributing to the pressure changes within the channel. An analysis of the pressure at the inlet and outlet showed that the mass flux effect on the frequency of reverse flow and two-phase mixing events varied depending on inclination. The nucleation site location substantially affected the instability frequency at an inclination of +30°. Channels inclinations of 0°, +30°, +45° and +60° experienced the most instability-driven cooling, while at +90°, instabilities reduced as bubbles were eased toward the channel outlet via buoyancy. For horizontal and all of the upward inclined channels, the heat transfer improvements became more significant as heat flux increased. The results provide guidelines for how flow instabilities can enhance the heat transfer performance during flow boiling while at the same time avoiding surface dry-out.

1. Introduction

Heat removal from microelectronics is essential to ensure performance and protect against temperature runaway and burnout [1]. Flow boiling cooling is a promising active heat removal strategy whereby heat is transported away from microelectronic components via simultaneous bulk fluid motion and liquid-to-vapour phase change. However, the vapour itself, which has a relatively low heat absorption ability, can result in significant heat transfer inhibition when trapped on or confined at the diabatic surface, resulting in temporal flow instabilities.

Such instabilities disrupt the dominant steady-state mechanism, which can affect the heat transfer and, hence, the heat removal performance. Liquid–vapour flow patterns can be significantly altered and, in severe cases, can lead to temporary reverse flow of the vapour phase opposing the bulk fluid motion. Flow instability can produce oscillatory changes in the observed flow, such as bubble position [2], and/or mass flow rate [3], and/or pressure-drop [4] and/or heated surface temperatures [2] for both surface tension and buoyancy-dominated flow. Flow instability can result in excessive mechanical vibration, causing component damage and noise generation [5] or the prevalence of off-design heat transfer behaviour. To help understand flow instabilities which assist in overcoming or avoiding these drawbacks, this work focused on characterising the flow instability and quantifying its effect

* Corresponding author.
E-mail address: jaco.dirker@up.ac.za (J. Dirker).

https://doi.org/10.1016/j.ijheatmasstransfer.2025.127472
Received 6 March 2025; Received in revised form 8 June 2025; Accepted 26 June 2025
Available online 5 July 2025

Nomenclature

a	Correlation equation coefficient
A	Cross-sectional area (m^2)
b	Correlation equation exponent power
Bi	Biot number
Bd	Bond Number
c_p	Specific heat (J/kg·K)
Co	Confinement number
d_h	Hydraulic diameter (μm)
g	Gravity (m/s^2)
G	Mass flux ($kg/m^2 \bullet s$)
h_{fg}	Latent heat of evaporation (J/kg)
H	Flow passage height (m)
I	Electric current (A)
k	Thermal conductivity (W/m·K)
L_h	Heated surface length (m)
L_{cap}	Capillary length (m)
L_P	Periemeter length (m)
$\dot{m}$	Mass flow rate (kg/s)
n	Number of time steps
n_P	Number of pressure measurements above the threshold
P	Pressure (kPa)
P_f	Instability frequency (Hz)
P_{ins}	Instability categorise pressure measurement (kPa)
$\dot{q}$	Effective heat flux (W/m^2)
$\dot{Q}$	Absorbed heat (W)
t	Time (s)
T	Temperature (°C)
T_h	Heated surface temperature (°C)
U	Voltage (V)
$\dot{V}$	Volumetric flow rate (m^3/s)
W	Flow passage width (m)

Greek symbols

α	Heat transfer coefficient ($W/m^2 \cdot K$)
β	Inclination angle (°)
ϵ	Emissivity
ρ	Density (kg/m^3)
σ	Surface tension (N/m)
τ_w	Wall thickness (m)

Subscripts

0	Atmospheric condition
f	frequency
in	Inlet condition
ins	Instability
IR	Infrared
l	Liquid state
net	Net condition
out	Outlet condition
sat	Saturation condition
v	Vapour state
x	Axial position
y	Axial position
z	Axial position

on heat transfer performance in minichannels where the relatively high bubble-volume-to-channel-volume ratios result in amplified surface temperature effects [6].

Quantifying the frequency with which flow instability occurs and its impact on heat transfer performance is typically achieved by analysing the duration and magnitude of pressure and temperature signal changes. These signals can also be used to differentiate between the two main types of flow instability, which are either long-duration small-amplitude oscillations (static instabilities) or short-duration high-amplitude oscillations (dynamic instabilities) [7]. Static instabilities are identified by monitoring pressure-drop oscillations and have a period of between 120 and 600 s [8], which often affects the temperatures at the inlet, outlet, and on the heated surface [9]. These instabilities take the form of changes in flow patterns (such as from annular to mist flows) and depend on the level of bubble confinement, which can be identified as pressure-drop oscillations and density wave oscillations. Density wave oscillations are mechanistically described by Jung et al. [10], with the key defining features that the instability period is in the order of 2–6 s, that they are cyclic and are often initiated by bubble nucleation upstream of the vapour slug or the annular flow region. Dynamic instabilities are known as pressure-drop oscillations, which are described mechanistically by Qu et al. [11], with the key defining features being that the instability period is less than 2 s [8], that it occurs randomly rather than cyclically, and that the instability is observed as the vapour front recedes towards the inlet (reverse flow). In addition, reverse flow over a short distance is defined as a mild pressure-drop oscillation, while reverse flow up to the length of the channel into the inlet plenum is defined as a severe pressure-drop oscillation. Other forms of flow instability include fluid density wave variations, which result in thermal oscillations [12] on the heated surface, inlet, and outlet. Dynamic instabilities can cause wall temperatures to increase due to the rapid expansion of bubbles as liquid changes phase to vapour, which intensifies at higher heat flux conditions [13], particularly when nucleate boiling dominates [7].

The impact of dynamics instability on the heat transfer performance has been investigated extensively, with some experimental investigations observing premature dry-out on the heated wall [14], and/or flow regime changes [2], and/or reverse flow [11]. Dry-out is associated with a premature occurrence of the critical heat flux [15], which is generally undesirable and can be caused by pressure-drop oscillations [15]. Flow regime changes, for instance, from vapour slug flow to dispersed bubbly flow, can improve the heat transfer performance, while the opposite transition would reduce the heat transfer performance. Similarly, rapid vapour motion towards the inlet (reverse flow) can substantially reduce the in-channel heat transfer performance in some instances but can also lead to increased heat transfer performance if the thermal boundary layer disruption causes increased fluid mixing. Flow instability can thus not be classified as beneficial or detrimental to flow boiling heat transfer and must be investigated on a case-by-case basis.

Flow instability magnitude, frequency and impact can be suppressed by increasing the mass flux [16] or increasing the inlet pressure to overcome the flow resistance [17]. These factors change the pressure-drop across the channel, which is typically high in microchannels. Large pressure-drops across a channel (i.e., high flow resistance) lead to large variations in specific volumes of the vapour and liquid along the channel length, increasing the likelihood of flashing [18]. Changing the inclination of the flow passage within a gravity field (i.e., a flow that is horizontal, upward, downward, or slanted) affects vapour containment in the channel and the inlet pressure. Upwards flows typically allow for vapour to easily escape the channel eased by bubbles buoyancy and increase the inlet pressure, decreasing flow instability [20], whereas downward flows can trap vapour in the channel and decrease the inlet pressure, leading to increased flow instability [19]. In fixed orientation systems, such as in server rooms, the cooling inclination can be selected to minimise the likelihood of flow

instability and flashing. Mass and heat flux affect the likelihood of flow instability, with experimental observations used to map regions of relatively stable and unstable flow on instability maps. Flow instability observations can also be used to create flow regime maps and dry-out maps [18].

Temperature variations on the heated surface due to dynamic instabilities often require spatial and temporal high-resolution measurements to be accurately captured. The choice of the heating method determines the accuracy and resolution with which changes in the heated surface can be captured. The most common heating method uses a large metal block with cartridge heaters placed in the base, with surface temperatures monitored by evenly spaced thermocouples close to the surface of the channel. Clark et al. [20] experimentally investigated flow boiling of Hydrofluoroether (HFR-7100) through channels with square-cross-section channels ranging between 0.25 and 1 mm in width at mass fluxes from 100 to 1600 kg/m^2•s and found little effect of dynamics instabilities. This study used cartridge heating, supplying one-sided heating, and the authors reported that the minimal impact of the dynamic instabilities on the surface temperature was possibly due to the thermal capacity of the metal block dampening the temperature response. On the other hand, sputtering is a technique where a visually semi-transparent layer of metal, such as Tantalum or Indium Tin Oxide, is applied to one or more sides of a borosilicate channel [9,21]. This layer supplies ohmic heating for fluid heating and infrared thermographic measurements, while its transparency in the visual spectrum allows for high-speed image capture [22]. Flow instability can then be captured using thermographic and visual observations, as well as inlet and outlet fluid temperature and pressure changes. Inlet and outlet temperature changes are typically measured using in-flow thermocouples, while differential or independent pressure transducers measure the inlet and outlet pressure response.

Differential pressure transducers identify long-duration oscillations, while independent pressure transducers identify short-duration oscillations at the inlet or outlet. Using differential pressure transducers, Cheng et al. [79] differentiated between stable and unstable flow boiling in a heat sink with 14 parallel microchannels, each with a hydraulic diameter of 86.3 μm. The working fluid was deionised water with heat fluxes from 7.9 kW/m^2 to 87.7 kW/m^2 at mass fluxes from 22 kg/m^2•s to 44 kg/m^2•s. The study aimed to present the difference in flow pattern during two-phase boiling under stable and unstable flow conditions. The total pressure-drop was an accurate method to identify reverse flow. The total pressure-drop was calculated using the maximum and minimum instantaneous pressure-drop at any point in the experiment. A pressure-drop greater than 6 kPa was indicative of reverse flow. This threshold pressure was defined by comparing the pressure response and visual observations. On the other hand, Hedau, et al. [19] used independent and differential pressure transducers in a cartridge heating arrangement of 10 parallel microchannels with a width of 315 μm and height of 600 μm at inclinations of vertical upwards flow, vertical downwards flow, horizontal heated from below and horizontal heated from above. Heat fluxes tested ranged from 230 kW/m^2 to 2200 kW/m^2 at a mass flux of 250 kg/m^2•s. Flow instability was found to negatively affect the heat transfer performance, with an increase in the inclination decreasing the magnitude of the impact. Vertical downward flow produced the worst heat transfer performance with the most severe reverse flow, while vertical upward flow was the least impacted by reverse flow and had the best heat transfer performance. Cheng and Xu [23] also investigated flow boiling in 14 parallel microchannels, each with hydraulic diameters of 114 μm with deionised water at mass fluxes from 446 kg/m^2•s to 963 kg/m^2•s and heat fluxes from 175 kW/m^2 to 4072 kW/m^2. Flow instability negatively impacted heat transfer performance due to the high-temperature fluid in the two-phase region moving towards the channel's inlet, increasing the average bulk fluid temperature. It was also found that the subcooling level (the temperature at which the fluid enters the channel) substantially affects the severity of flow instability. Flow instability severity was reduced by increasing the subcooling temperature.

Flow instability negatively impacted the heat transfer performance in the three studies above. Several other studies had similar findings [27–29], where the primary cause of decreased performance was flow maldistribution in multichannel systems and higher fluid temperatures close to the inlet due to reverse flow. Flow instability has, however, also been observed to improve heat transfer performance, as was found in a study by Chen and Garimella [24]. In their study, flow boiling of Perfluorocycloether, FC-77, was investigated via 60 parallel microchannels with a width of 100 μm and a depth of 389 μm at mass flow rates between 253.7 kg/m^2•s and 1015.0 kg/m^2•s and heat fluxes between 305 kW/m^2 and 623 kW/m^2. It was found that flow instability caused little change in the heat transfer coefficient around the nucleation site in the centre of the channel. However, heat transfer rates upstream and downstream of the nucleation site were found to be enhanced by instability events. Changes in the flow pattern were credited with heat transfer performance improvements. This suggests that when the mass flow rate is low enough, heat transfer can be enhanced by instability events. Maciejewska et al. [25] also found an increase in the heat transfer coefficient in the most unstable portions of the boiling curve. Their experimental investigation considered FC-72 boiled in two parallel minichannels, each with a depth of 1.7 mm, a width of 16 mm, and a length of 180 mm. Heat fluxes from 0.0 kW/m^2 to 19.0 kW/m^2 were studied at a net mass flux of 163 kg/m^2•s. The heat transfer performance was determined using infrared surface temperature analysis. The best heat transfer performance was found around the incipience of boiling via nucleation hysteresis. The flow was most unstable at the onset of boiling, and was characterised by both static and dynamic instabilities. This study suggests that a heat transfer coefficient improvement of up to 700 W/m^2•K can be achieved at mass fluxes of 163 kg/m^2•s.

The location and number of the nucleation sites can greatly influence flow boiling heat transfer. Mastrullo et al. [26] experimentally investigated the flow boiling of R452A in a 6 mm diameter circular channel at mass fluxes from 150 kg/m^2·s to 600 kg/m^2·s and heat fluxes from 10.0 kW/m^2 to 65.0 kW/m^2. The heat transfer performance decreased as vapour quality increased due to temperature glide, where the saturation temperature of the fluid increased with vapour quality. This effect on the channel bubble dynamics hinders nucleation site formation, which results in a reduced heat transfer rate. Nucleation site location can, at times, be difficult to identify, as was found by Menezes et al. [27]. The study considered CO_2 in a 4.57 mm diameter circular channel and a 2 mm cross-sectional area square multichannel system at mass fluxes between 140 kg/m^2·s and 1000 kg/m^2·s at heat fluxes up to 85.0 kW/m^2 and pressures between 2 and 4 MPa. A high-speed camera with a frame rate of 1000 fps was placed below the channel and could consistently identify nucleation sites within the liquid film at low vapour qualities. At higher vapour qualities, the nucleation site location had to be inferred. It was found that when the number of nucleation sites decreased, the heated surface temperature increased, reducing the heat transfer rate. More recently Bian et al. [28] experimentally investigated flow boiling in multichannel systems with smooth and rough surfaces. The study considered flow boiling at mass fluxes of 13.8, 230.3 and 331.9 kg/m^2·s through a channel with a width and height of 2mm and inlet tempeartures between 70.0 and 80.0 °C. It was found that the heated surface temperature required to sustain boiling was lower for rougher surfaces than for smooth surfaces. The lower heated surface temperature produced a heat transfer improvement of up to 18 % higher for the rough channel compared to the smooth channel due to the ease with which nucleation sites formed.

Experimental investigations of flow-boiling in single or multiple minichannel systems have predominantly been at a horizontal orientation. Inclination effects on flow instability with single-sided heating have rarely been studied experimentally. Still, some evidence suggests that under the same heat flux and mass flux conditions, positive inclinations have a decrease in the heated surface temperature due to flow instability, while horizontal channels have an increase in the heat

surface temperature, which is demonstrated in this work. Other studies have also shown that the heat transfer rate is improved at vertical inclinations compared with horizontal inclinations [29]. Some studies have shown that flow instability can benefit heat transfer performance and that low flow inertia and high heat fluxes can exacerbate flow instability by resulting in larger temperature and flow effects [17]. In addition, Perfluorohexane (FC-72, C6F14), a highly suitable refrigerant for electronic cooling, which has not yet been extensively investigated, is used in this work. It is thermally and chemically stable, electrically inert, non-flammable, non-toxic, and leaves no residue upon evaporation [30].

The novelty of this study is the investigation of vapour buoyancy effects at different inclinations under non-uniform heat flux, i.e., single-side heating, which has not yet been well defined during dynamic flow boiling, and which is important in microelectronic applications. For this purpose, a single rectangular micro-/mini-channel scenario was considered under single-side heating at inclinations from partial negative to horizontal and positive cases up to vertically upwards flow. The channel had a rectangular flow passage with an aspect ratio (width-to-height) of 10 and a hydraulic diameter of 909 μm. Because the vapour buoyancy effects at the intermediate inclinations are not well defined during dynamic flow boiling, this study produces relevant experimental data at various mass flow rates, heat fluxes and inclination angles using FC-72. Flow instability patterns, surface temperature effects, and their impact on the channel pressure-drop were investigated using high-speed camera, infrared camera surface temperature mapping, and independent pressure transducers. An emphasis was placed on determining whether pressure transducer data resulting from flow instabilities can be used to predict the surface temperature changes and/or heat transfer performance variations. Because it has been shown that low flow rate conditions are more susceptible to flow instability, mass fluxes from 10 $kg/m^2 \bullet s$ to 40 $kg/m^2 \bullet s$, so to minimise inertia effects, at heat fluxes between 4.3 kW/m^2 and 21.7 kW/m^2 were investigated. Inclination effects were studied by performing experiments at channel orientation that included slanted downward flow, traditional horizontal flow, several upward inclined cases, and finally vertical upward flow.

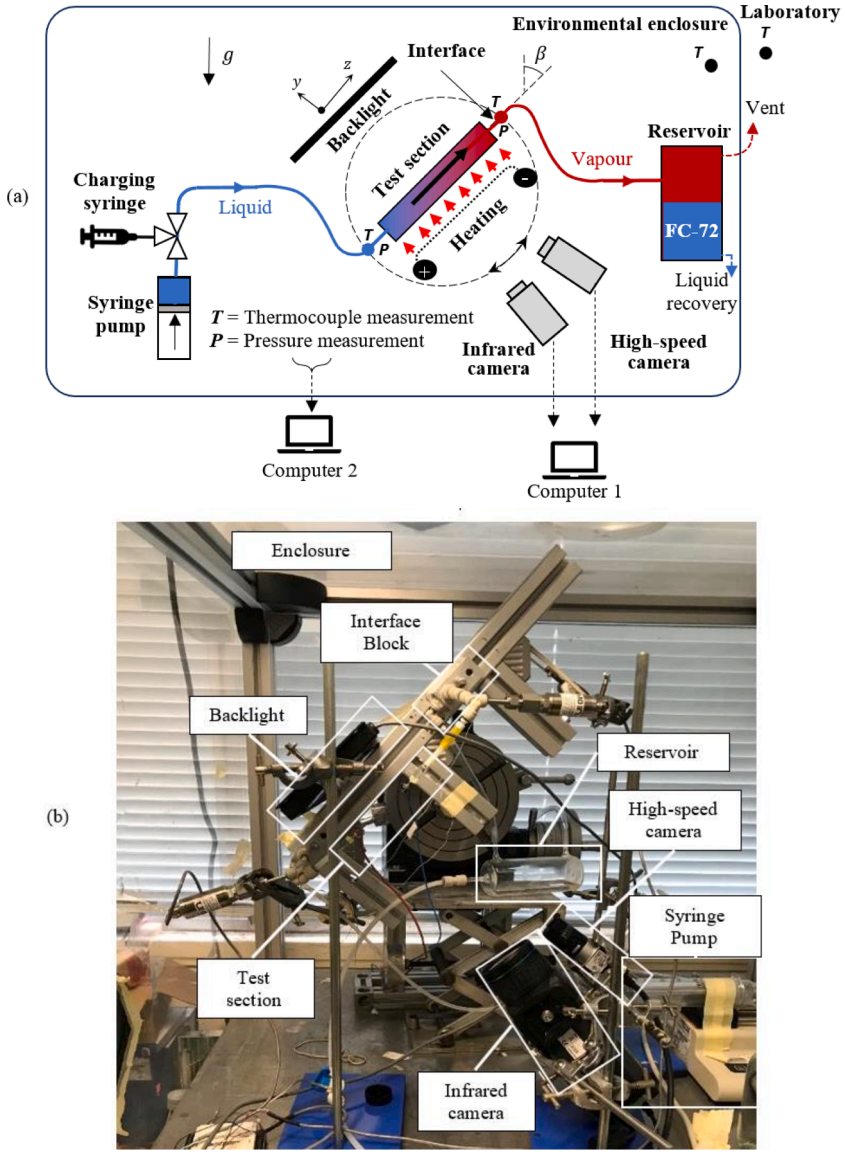

Fig. 1. (a) Schematic representation of the experimental equipment's flow path starting with the syringe pump and charging syringe, followed by the inlet interface, test section and outlet interface where all sensory equipment is connected, and lastly, the reservoir where the vented two-phase fluid or vapour is then collected. (b) A snapshot of the full experimental setup for an inclination $\beta = +45^\circ$ and bottom-side heated experiment. Fluid moved through the test section from bottom left to top right.

2. Experimental facility

2.1. Experimental equipment

Fig. 1a and b, respectively, provide a schematic representation and photo of the experimental equipment. It consisted of a syringe pump supplying Perfluorohexane (FC-72) to a test section heated electrically at a range of inclination angles (β) and a collection reservoir open to the atmosphere.

The components in Fig. 1a include a KDS® 100 Screw-thread syringe pump consisting of a glass cylinder with a maximum volume of 100 ml and an internal diameter of 34.20 mm (± 0.02 mm). It had a flow range from 0.1 µl/h to 506 ml/hour (with an accuracy of ± 1 %). The fluid delivery rate was controlled by changing the speed at which the plunger was depressed, ensuring a constant volumetric flow rate. The working fluid was filled through a charging syringe connected to a three-port valve after the discharge point from the syringe pump via flexible tubing. Thermally uninsulated flexible tubing (approximately 500 mm long and 3 mm in diameter) supplied the fluid to a thermally uninsulated rigid metal block approximately 20 mm long with a 5 mm internal diameter before entering the test section.

The test section was mounted to an Axminster® rotary table via two identical interfacing assemblies (one each at the inlet and outlet). Fig. 1b shows the mounting for an upward inclination case of +45° (the fluid enters the test section at the bottom left and moves to the top right). A dial with a 1° resolution indicated the inclination angle, and fasteners were used to lock the system in place for the duration of the tests. Besides enabling mounting, each interface assembly (which will be described in more detail later) allowed for the measurement of the temperature and pressure of the fluid at the inlet and the outlet.

After the test section, an uninsulated rigid and flexible tubing from the outlet interface condensed the FC-72 before being collected in the 350 ml outlet reservoir. Collected fluid was drained and stored in airtight containers if it was needed for degassing. The reservoir was vented to the atmosphere, keeping the experimental facility at an atmospheric pressure of approximately 101 kPa.

A 1 m by 1 m by 1 m acrylic glass enclosure shielded the facility from bulk air motion and infrared reflections from other equipment in the laboratory. The enclosure temperature was monitored with a K-type thermocouple, while a secondary K-type thermocouple monitored the temperature outside the enclosure. CCD and IR cameras were also contained within the enclosure and were used to capture images of the bubble dynamics and the single-sided heated wall surface temperatures.

Details of the test section are given in Fig. 2a and c, while the interface assembly at the outlet, which is similar to that of the inlet (but not shown), is given in Fig. 2b. As mentioned, the inlet and outlet assemblies were identical, enabling pressure and temperature measurements. Each assembly consisted of an l-shaped push-pull fitting and a T-shaped push-pull fitting (PEM0310W John Guest®). The latter connects to an Omega® PXM219 pressure transducer (one at the inlet and outlet), with a full-scale range of 0 to 250 kPa and measurement accuracy of 0.025 % [31]. The pressure transducer had a port length of 5 cm, the distance from the T-shaped push-pull fitting to the l-shaped push-pull fitting was 4 cm, and from the l-shaped push-pull fitting to where heating began on the test section was 9 cm. See Fig. 2 for a schematic showing the position of the l-shaped and T-shaped push-pull fittings. The outlet pressure transducer was at a similar distance from the end of the channel's heated length. Although these distances could result in some of the pressure fluctuations not being effectively captured by the pressure transducers, it would be a flow phenomenon that is not consequential for the heated surface temperature, as is discussed in Sections 5.5 and 5.7.

A K-Type thermocouple (tip diameter of 1 mm) was threaded through a 2.00 mm hole in the l-fitting (Fig. 2d), allowing for full immersion in the fluid for the duration of all the experiments, with the tip placed at the centre of the glass end cap. The hole through the l-shaped fitting was sealed using the same Araldite® Rapid epoxy.

Now, considering the test section itself, as stated in the introduction, horizontal channels heated from below typically had better heat transfer performance than when heated from above [32,33]. Thus, the present work considered a width-wise horizontal test section heated from below at different inclinations. Each test section consisted of an extruded high

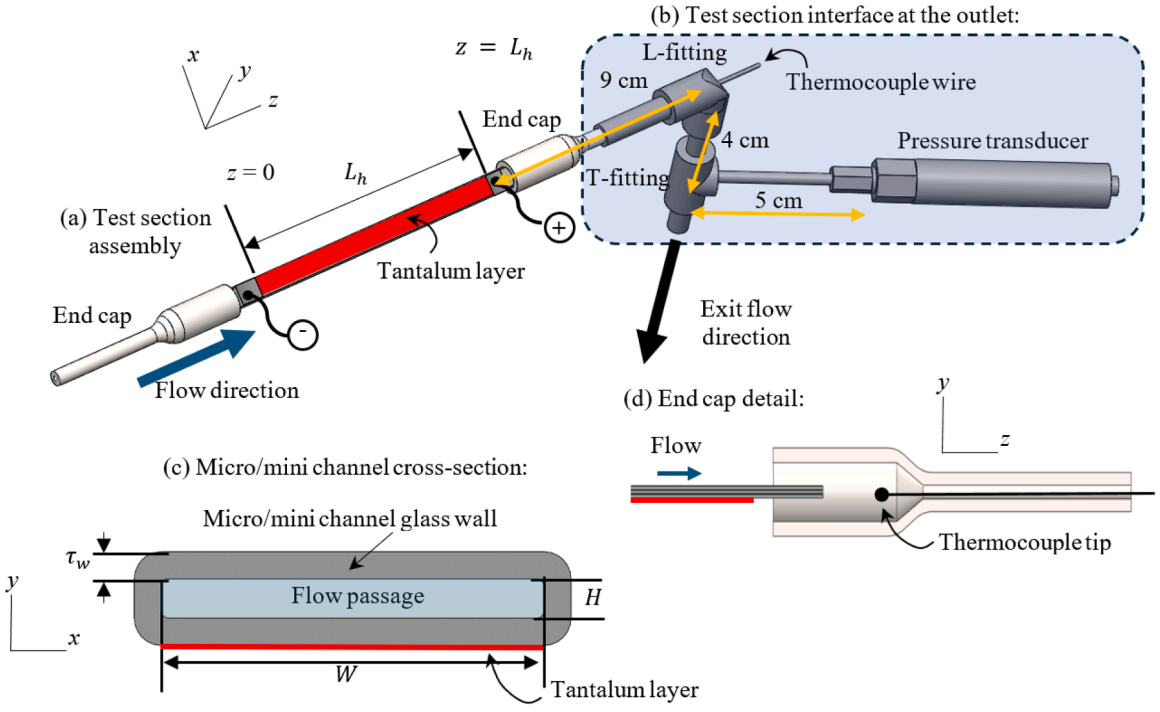

Fig. 2. Schematics of (a) fully assembled Tantalum-coated test section, (b) test section interface connected to the channel outlet (identical to the one connected at the channel inlet), (c) cross-sectional view of minichannel with the Tantalum coating at the bottom of the channel and (d) end cap detailed view.

aspect ratio borosilicate glass channel attached to circular glass-blown end-caps via Araldite® Rapid epoxy with a melting temperature of 80.0 °C. The end-caps (Fig. 2d), which enabled connection to the inlet and outlet interface assemblies, each had an axial length of 30.00 mm, an inner diameter of 6.00 mm on the test section end, and an inner diameter of 3.00 mm on the interface assembly side.

Vitrocom™ supplied the borosilicate glass channels (Fig. 2a and c). Multiple identical channels were created to account for channel breakages during test section creation and breakages during test section installation and inclination adjustments. Two channels were used in this study, one for inclinations of $\beta = -20°$, $-15°$ and $-10°$, and a second for $\beta = 0°$, $+30°$, $+45°$, $+60°$ and $+90°$ This ensures homogenous and repeatable conditions within the microchannels for the different parameters studied. Each channel had an axial length (L) of 100.00 mm ± 0.02 mm in the z direction, a flow passage width (W) of 5.00 mm ± 0.02 mm in the x direction, and a flow passage height (H) of 0.50 mm ± 0.02 mm in the y direction. The wall thickness (τ_w) was 0.35 mm (± 0.02 mm) and was uniform along the channel length.

The hydraulic diameter of 909 μm, $d_h = 4 \cdot \frac{A}{L_P}$, was calculated using the wetted cross-sectional surface area A, and the wetted perimeter L_P. The aspect ratio is the width W to height H of the channel ratio and equals 10 for the test section chosen. Channel size classifications were based on whether micro-, mini- or macro-scale physics would dominate the bubble behaviour. The Laplace constant ($L_{cap} = \sqrt{\frac{\sigma}{g(\rho_l - \rho_v)}} \approx 780\ \mu m$) or capillary length is a threshold hydraulic diameter calculated using surface tension σ, gravity g, density of the liquid ρ_l and vapour ρ_v phase. Microchannel physics dominates when $d_h < 0.224L_{cap}$, minichannel physics dominates when $0.224L_{cap} < d_h < 1.75L_{cap}$ and macrochannel physics dominate when $1.75L_{cap} < d_h$ [34]. Two non-dimensional numbers, the Confinement number ($Co = \frac{1}{d_h}\sqrt{\frac{\sigma}{g(\rho_l - \rho_v)}} \approx 0.861$) and Bond number $\left(Bd = \frac{g(\rho_l - \rho_v)d_h^2}{\sigma} \approx 1.34\right)$ can be used to further classify the channel by additionally considering fluid properties. The dominating physics for Confinement numbers greater than 1.0 would be microchannel physics [35], numbers less than 0.4 indicate macrochannel physics [36], while numbers between 0.4 and 1.0 indicate the transition period where minichannel physics would dominate [36]. Meanwhile, Bond number $Bd > 3.0$ indicates macrochannel physics, numbers between $0.5 < Bd < 3.0$ indicates minichannel physics while $Bd < 0.5$ indicates microchannel physics, and less than 3 indicates that minichannel physics dominates [16,34]. These numbers all suggest that a mixture of surface tension-driven and buoyancy-driven effects would be observed.

For a 5 mm by 0.5 mm channel, the hydraulic diameter, Laplace constant, Confinement number and Bond number are given in Table 1. The $0.224L_{cap}$ (175 μm) and $1.75L_{cap}$ (1370 μm) diameters are calculated as shown alongside the channel size category ranges. It is shown that the hydraulic diameter falls between the upper and lower limits of minichannel physics, suggesting both surface tension and buoyancy forces would be expected. In all classification cases, a mixture of surface tension and buoyancy forces are expected to affect the flow behaviour, indicative of minichannel physics.

To produce single-sided heating, a 22.5 nm layer of Tantalum was sputtered onto one of the outer flat walls of the glass channels at the Scottish Microelectronics Centre (SMC). This thin metal layer was visually transparent and had sufficient mass to facilitate electrical heating, allowing infrared surface temperature measurements as well as flow visualisation. Prior to the Tantalum coating process, the test sections were cleaned before sputtering; impurities and biological agents were removed by submerging the channels in a sulphuric acid and hydrogen peroxide solution for 30 min and then rinsing them with deionised water. After that, the test sections were thoroughly dried to ensure no Tantalum clumps or Tantalum free zones were present on the channel surface. Drying was a two-step process starting with passing high-pressure air through the inside and over the outside of the channel; the test sections were then placed in an oven for further drying. Last, Tantalum sputtering on one side of the channel was carried out using an Oxford Instruments® Plasmalab System 400 inside a Class 10 cleanroom, allowing all channels to be coated simultaneously.

Electric terminals were obtained by wrapping either end of the minichannel with aluminium foil and connecting it via clamps to an adjustable Clairtronic® VARIAC direct current (DC) rectifier. Depending on the location of the aluminium foil, the heated length ranged from 75.00 to 80.00 mm (± 0.02 mm), and the electrical resistance was typically 3.75 kΩ.

2.2. Data acquisition

Flow visualisation and bubble dynamics were captured with a Basler® acA800–510um. This high-speed CCD camera has a resolution of 800 × 600 pixels and can capture images at 511 frames per second (fps). A 12 mm fixed lens was used, and images were captured at 140 fps. Pylon Viewer® controlled the camera's settings, and the individual images could be retrospectively combined and analysed using a custom-built MATLAB® script.

Surface temperature mapping was done using a FLIR® A645 infrared camera placed inside the enclosure. The camera had a thermal sensitivity of 20 m·K, a 640 × 480 pixels resolution, a maximum frame rate of 25 fps and a detection range between −40.0 °C and 150.0 °C. Self-reflection was eliminated by directing the camera at a 5° orthogonal offset. A non-reflective sheet was placed on the enclosure's metal floor to prevent interference from this surface. Video recordings were processed by using ResearchIR® software.

A National Instruments® data acquisition system with a SCXI-100 chassis and a SCXI-1303 data card was used to capture thermocouple signals, while a stand-alone Data acquisition DAQ, National Instruments USB-6008, captured the pressure transducer data. Both systems collected data at 100 Hz.

The current and voltage of the DC power supply were measured using two MASTECH® MS8239 multimeters with typical readings in the tens of mA and tens to hundreds of V. The uncertainty of a current measurement was 1 % of the measured value +1 mA. The uncertainty of a 40 mA measurement would be 0.4 mA for the percentage uncertainty and 1 mA uncertainty from the absolute uncertainty for a total uncertainty of 1.4 mA. The voltage measurement had an uncertainty of 0.5 % + 0.2 V. The uncertainty of a 100 V measurement would be 0.5 V for the

Table 1
Summary of channel classification sizes for the 5 mm by 0.5 mm channel.

Channel dimensions (mm)	Aspect ratio	Hydraulic diameter (μm)	Laplace constant (μm)	Confinement number	Bond number
5 mm by 0.5 mm	10	909	Microchannel $d_h < 0.224L_{cap}$ $0.224L_{cap} = 175$ Minichannel $0.224L_{cap} < d_h < 1.75L_{cap}$ $1.75L_{cap} = 1370$ Macrochannel $1.75L_{cap} < d_h$	0.861	1.34

percentage error and 0.2 V for the absolute error, totalling 0.7 V.

3. Method

3.1. Sensor calibration

An OPTIMA® T100 thermal bath filled with deionised water was used to calibrate all the thermocouples before the first experiment. Calibration temperatures were increased from 20.0 °C to 60.0 °C in 5.0 °C intervals with only steady-state data recorded. After completion of all experiments, the thermocouples were assessed for calibration drift, with none observed.

A SPER SCIENTIFIC® Model 84083 manometer was used to calibrate the pressure transducers at gauge pressures from 0 kPa to 200 kPa. During calibration and operation, pressure transducers were oriented such that the port lead was higher than the pressure probe, ensuring it was always filled with liquid and air/vapour and would not invalidate the data. The orientation of the pressure transducers during operation and calibration was the same to minimise hydrostatic effects.

Infrared temperature measurements require four parameters. The first two are the temperatures of the environment and the reflective surfaces, taken as the temperature inside the enclosure. The other two are relative humidity, which ranged from 38 % to 45 % between experiments, and the distance between the test section and the infrared camera, measured using a Vernier Calliper at around 20.00 ± 0.01 mm. These parameters changed the air's transmissibility by around 1 %, negligibly affecting the measured surface temperature measurement [37]. Emissivity was the most important input, determined using a technique developed by Madding [38], where the temperature of the test section was measured using an infrared camera and a calibrated thermocouple. The tantalum surface's emissivity was determined by setting the infrared camera's emissivity to 1.0, a black body. A thermocouple was then placed in contact with the tantalum layer. The surface's temperature was first measured at room temperature (16.0 °C) and then after the enclosure was heated to 35.0 °C. The 4 temperature measurements were used to determine the emissivity of the tantalum layer using:

$$\epsilon = \frac{T_{IR2}^4 - T_{IR1}^4}{T_{h1} - T_{h2}} \tag{1}$$

where, ϵ is the tantalum's emissivity, T_{IR1} and T_{IR1} are the infrared camera's temperature measurements for the first and second tests (16.0 °C and 35.0 °C), and T_{h1} and T_{h2} are the heated surface's temperature measured by the thermocouple for the first and second tests (16.0 °C and 35.0 °C). The emissivity calculated was approximately 0.79, which aligned well with other studies using Tantalum [39–42].

The infrared camera's temperature measurement was verified against a surface with a known emissivity at two isothermal conditions, the first at room temperature (16.0 °C), and the second after a convective heater was used to increase the temperature in the enclosure to 35.0 °C. Electrical tape with a known emissivity of 0.95 was wrapped around the minichannel, with a thermocouple placed in contact with the surface. The infrared camera's emissivity was set to 0.95. Temperatures from both the infrared camera and the thermocouple were recorded at 16 °C and 35 °C. The heated surface temperature was correctly measured, with both temperature measurements within 0.2 °C of each other.

Now that the emissivity of the Tantalum layer was known and the camera's temperature measurements were verified, an isothermal test was performed where the test section was unheated, but fluid was delivered to the minichannel and with the infrared camera's emissivity was set to the measured 0.79. The surface temperature was the same as the inlet and outlet thermocouple temperature, as no heating was applied. The measured infrared camera temperature was uniform across the surface and the same as the inlet and outlet thermocouple measurements. This test validated both the Tantalum's emissivity and the infrared camera's ability to detect the surface temperature accurately. Under these isothermal conditions, the inlet and outlet thermocouple measurements were compared with the infrared unheated surface temperature measurements, where it was found that the standard deviation of the infrared measurement was 0.18 °C with no shift when an emissivity of 0.79 was used. Although the infrared camera's measurement uncertainty was ± 2.0 °C, these observations gave confidence in decreasing the uncertainty in the infrared temperature measurements from ± 2.0 °C to ± 0.18 °C.

Volumetric flow rates from the syringe pump were verified manually by having a beaker and measuring the total ejected flow in time at 50, 100 and 200 ml/h. The volume of water collected was compared to the expected value based on the syringe pump's flow rate setting and the time elapsed. The syringe pump volumetric flow rate was within ± 1 % of the measured output.

3.2. Test parameters

As stated, FC-72 was used in this study. The inlet temperature (T_{in}) followed that of the laboratory temperature T_0 and ranged from 18.0 °C to 19.5 °C. The FC-72 saturation temperature (T_{sat}) was measured and ranged from 55.5 °C to 56.3 °C, due to changes in atmospheric pressure inside the microchannel/test section. The inclinations (β) ranged from −20° (negatively inclined) to 0° (horizontal) to +90° (fully vertical). The channel's heated length (L_h) was 64.00 mm for negatively inclined channels and 80.00 mm for horizontal and positively inclined channels. Negatively inclined channels had a shorter length due to channel breakages, which reduced the number of available channels.

Channel inclinations of β = 0°, +30°, +45°, +60° and +90° were tested at mass fluxes of 10 kg/m^2•s, 20 kg/m^2•s and 40 kg/m^2•s. While β = −10° was additionally tested at a mass flux of 20 kg/m^2•s, and β = −10°, −15° and −20° were also tested at a mass flux of 40 kg/m^2•s. These negative inclinations could not be tested at all mass fluxes as the bubble buoyancy resulted in vapour motion into the inlet plenum during a steady state at 10 kg/m^2•s. This caused complete dry-out and local overheating of the test section. Table 2 summarises the test matrix and includes the applied heating rates and the net heat flux condition on the channel wall after considering thermal losses.

3.3. Procedure

A horizontal reference position in the *y-z* plane was adopted for the test section from which all other inclinations were defined. The distance from the metal base plate inside the acrylic glass enclosure to the inlet and outlet of the channel was measured to determine when the channel was horizontal. The base plate was determined to be horizontal using a spirit level. From this position, the dial-operated rotary table adjusted the inclination of the test section to the desired position.

Testing began with single-phase experiments to determine the heat lost from the channel to the environment. The total absorbed heat in the two-phase region can theoretically be determined using vapour quality, which requires complex techniques and expensive, unavailable equipment. This challenge was overcome by applying a homogenous

Table 2
Experimental parameters ranges tested at each mass flux.

Experimental Parameter	Value		
Mass fluxes (G)	10 kg/m^2•s	20 kg/m^2•s	40 kg/m^2•s
Net heat input ($\dot{Q}_{net}$)	2.7–6.0 W	3.7–8.2 W	5.3–10.2 W
Effective heat flux ($\dot{q}$)	4.3–11.3 kW/m^2	5.9–15.5 kW/m^2	10.4–21.7 kW/m^2
Inclinations tested	0°, +30°, +45°, +60°, +90°	−10°, 0°, +30°, +45°, +60°, +90°	−20°, −15°, −10°, 0°, +30°, +45°, +60°, +90°

equilibrium model to the test section, which defined an energy balance where the heat applied to the test section was accounted for with heat losses from the test section and heat absorbed by the fluid. This one-dimensional approach assumed a negligible amount of heat was lost through the test section and end caps, while heat losses from the heated wall dominated while heated losses from the three unheated faces were negligible. Several earlier heat transfer experimental works have successfully utilised and validated this one-dimensional approach or single-sided heating assumption [43–48].

The infrared camera captured the heated surface temperatures, and a thermocouple captured the environmental temperature in the enclosure during the single-phase experiments. These were used to calculate heat losses from the test section as a function of the temperature difference between the heated wall and the environment. The amount of heat absorbed was determined using the fluid's temperature at the inlet and outlet and the mass flow rate, while the applied heat was directly calculated using the current and voltage measurements from the multimeters. Several applied heat fluxes were tested at each inclination to create a correlation between heat loss and the environmental temperature difference (ΔT). This correlation was then used for all mass and heat fluxes tested in the two-phase experiments. The minimum heat flux applied to single-phase tests was when the outlet temperature was approximately 5.0 °C higher than the inlet temperature. The difference in temperature between the outlet and the inlet increased in 5.0 °C increments until the outlet temperature reached 55.0 °C, which is 1.0 °C less than the theoretical FC-72 saturation temperature T_{sat}. Single-phase heat loss tests were conducted at all 3 mass fluxes with at least 8 set points tested per mass flux. During the single-phase tests, steady-state conditions were defined as when the outlet temperature changed less than 0.2 °C for 3 min.

Correlation curves were created by correlating the heat loss to the environmental temperature difference at all three mass fluxes ($\dot{G}$ = 10 kg/m^2•s, 20 kg/m^2•s and 40 kg/m^2•s). Each inclination had its own correlation and was used to determine the effective heat fluxes by considering the amount of heat absorbed by the fluid. Two-phase experiments were conducted on the same day as the single-phase experiments at each inclination to avoid laboratory or atmospheric conditions impacting experimental results.

Before the two-phase experiments, the flow loop was charged with fluid using the three-port valve between the syringe pump and the inlet interface. Fluid was first added to the syringe in the syringe pump and then to the rest of the system. By forcing fluid through the system at flow rates much higher than the mass flow rates used in the experiment, trapped bubbles could be removed. Furthermore, the orientation of the pressure transducers was such that the probes were below the tubing, ensuring that vapour in the probes would move up into the tubes rather than stay in the transducer and affect the results.

Two-phase experiments started by initiating fluid flow from the syringe pump with no heating applied until fluid was seen collecting in the outlet reservoir. The applied heat was then gradually increased, protecting the system from flashing, which could cause local dry-out within the heated length of the test section and burnout of the Tantalum coating. Secondarily, increasing the heat flux rapidly could result in flow instability, leaving more nucleation sites closer to the inlet than what would typically occur from a gentle transition, i.e., low superheating conditions. The lowest heat flux tested during the two-phase experiments resulted in the onset of nucleate boiling. The onset of nucleate boiling was defined as sufficient heat applied to sustain an active nucleation site at all times within the heated surface. The heat flux was then increased in 10 V increments until surface temperatures of 150.0 °C was reached. The 150.0 °C limit protected the Tantalum layer from burning out and ensured temperatures remained within the calibration range of the infrared camera. The 150.0 °C limit for $\beta = +45°$, $+60°$ and $+90°$ was only reached at heat fluxes siginficantly higher than those tested for $\beta = -20°$, $-15°$, $-10°$, $0°$ and $+30°$ This was due to high heat transfer coefficients and mass transfer effects (discussed later), in which case, the maximum heat flux was determined through maximum tested voltages from other inclinations studied. Testing heat fluxes greater than the maximum tested at other inclinations was not valuable as this study's basis was to compare the flow instabilities and surface temperatures between inclinations at similar heat fluxes. Thus, the maximum number of heat fluxes tested at an inclination and mass flux combination was seven, and the minimum was three. Only three heat fluxes were tested at an inclination of $\beta = -20°$ as higher heat fluxes produced too large a buoyancy force in the two-phase region, resulting in complete dry-out.

Quasi-steady state conditions were determined by inspection of the outlet temperature and maximum surface temperature. Variations of less than 0.2°C for 3 min in the outlet temperature (time integrated averaged over 3 min), and maximum surface temperatures that changed cyclically indicated quasi-steady conditions during the two-phase experiments. Typically, surface temperature profiles reach quasi-steady conditions long before the outlet temperatures. Experiments were 60 s long, spanning from before an experiment began to after the experiment finished, and high-speed images were captured at between 100 and 140 fps for 70 s. Initial investigations showed that only short-duration oscillations occurred, typically less than 2 s in length, ensuring that a 60 s long experiment sufficiently captured all the phenomena of interest. Recordings from the infrared camera at 25 fps spanned 60 s, and the first frame of the infrared videos was determined to be the start time of the experiment. Temperature and pressure transducer measurements were taken at 100 Hz and started before the first experimental run/test and ran continuously until the end of a further 2 repetitions of the same experiment. This procedure of conducting 3 consecutive experiments took approximately 7 min.

4. Data processing

The infrared camera data determined the time stamps associated with the beginning and end of each repetition at an inclination, mass flux and heat flux combination. A MATLAB® code was used to align the start times of the infrared images, temperature data, and pressure data for each repetition. High-speed images were compared to the other data types manually. The data acquisition rate of the thermocouples and pressure readings was four times faster than that of the infrared camera. The surface temperature at the intermediary time steps was calculated by assuming a linear variation in temperature change between time stamps. This section presents the analysis of the heated surface temperature, effective heat flux calculations, pressure instability frequency characterisation and the measurement uncertainty analysis.

4.1. Heated surface temperatures

Each infrared image consisted of approximately 25 by 400 pixels corresponding to the heated surface region. Temperatures in the cropped region were evaluated via a MATLAB® script, mapping the outer heated surface $T_h(x,z,t)$ across the channel's width and length (x and z directions, respectively) at different moments in time (t).

For both the single-phase and two-phase experiments, the surface temperature was averaged across the channel width to produce the axial temperature profiles at different time stamps, $T_h(z,t)$. Instabilities were absent during the single-phase experiments, allowing further data averaging in time to produce the steady-state axial temperature profiles to enable the heat loss calculations. As will be shown later, the two-phase experiments were analysed using non-time averaged data, except when the effective heat flux and heat losses were calculated.

4.2. Heat flux

The homogenous equilibrium model was applied to calculate the time-averaged effective heat flux into the fluid $\dot{q}$:

$$\dot{q} = \frac{\dot{Q}_h - \dot{Q}_0}{L \cdot W} \tag{2}$$

Here $\dot{Q}_h$ and $\dot{Q}_0$ are the applied heating rate and heat loss rate to the environment, respectively, and L and W are the channel length and channel width, respectively.

A constant uniform heat flux applied by the electric heating, $\dot{Q}_h$, and was calculated as follows:

$$\dot{Q}_h = U \cdot I \tag{3}$$

where, U and I are the multimeter voltage and current readings.

The heat loss rate to the environment $\dot{Q}_0$ was calculated as follows:

$$\dot{Q}_0 = a[T_h - T_0]^b = a\Delta T^b \tag{4}$$

where T_h is the time and spatially averaged heated temperature from the infrared camera and T_0 is the time-averaged ambient laboratory temperature inside the acrylic glass enclosure. An environmental temperature difference was defined based on these two temperatures as $\Delta T = T_h - T_0$. $\dot{Q}_0$ is the amount of heat lost from the test section's heated length, and the power function parameters a and b, calculated during the steady-state single-phase experiments. This approach mirrors that of previous experimental investigations [43–48].

The single-phase experiments provided data under steady-state liquid-phase heating. This data was used to produce the power functions by calculating heat losses ($\dot{Q}_0$) which could be determined by performing an energy balance across the heated surface and considering the sensible heat of the fluid:

$$\dot{Q}_0 = U \cdot I - \dot{V}\rho c_P (T_{out} - T_{in}) \tag{5}$$

Here $\dot{V}$ is the pump's volumetric flow rate, ρ is the fluid density, c_P is the fluid's specific heat capacity, and T_{out} and T_{in} are the fluid's outlet and inlet temperatures measured by the inlet and outlet thermocouples. Heat loss curves for all inclinations and heat fluxes tested are shown in Fig. 3.

At each inclination, 15 data points were available as single-phase tests were conducted at 3 mass flow rates, with 5 heat fluxes each. This data was used to obtain the values of a and b in Eq. (4) via regression analyses. This produces 8 heat loss curves, one for each inclination with results from all heat flux and mass flux combinations included.

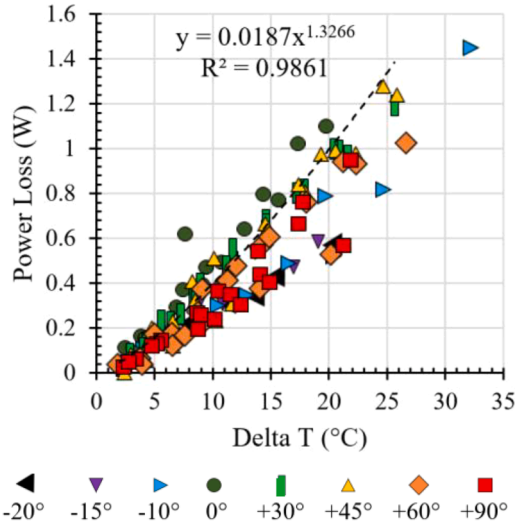

Fig. 3. Heat loss curves, $\dot{Q}_0$ (W), versus temperature difference ΔT (°C), for the channel at various inclinations, β (°), between −20° and 90°. The trend line is for +30° with a power function form of the equation given, including its coefficient of determination.

The power curve was found to produce the most accurate representation of the convective and radiative heat losses from the heated surface. The model had an accuracy of 1.5 % (or 0.1 W) for the liquid-only cases over the full temperature difference range between 5.0 °C and 32.5 °C.

The ratio of heat lost compared to the supplied power was inclination and heat flux dependent, ranging from 10 % to 50 %. The environmental temperature difference (ΔT) was a maximum of 32.5 °C during the single-phase experiments and up to 125.0 °C during the two-phase experiments. The high-resolution data with a large number of ΔT's investigated for each inclination allowed for an accurate power function curve.

Heat losses are dominated by natural convection. Several authors have found that the heat loss curves in a range of forms, including linear, non-linear, and exponential, from the lower end of the temperature range apply to the higher end [49–52]. Thus, the power curves were assumed to be valid in the two-phase temperature range.

FC-72′s properties are temperature dependent, and the manufacturer 3M® [30] has given several correlations for density and specific heat. The temperature used in the fluid property calculation was the time-averaged inlet fluid temperature:

$$\rho_l = 1740 - 2.61 T_{in} \tag{6}$$

$$\rho_V(1\ \text{atm},\ 56.0\ ^\circ\text{C}) = 13.2\,\text{kg}/\text{m}^3 \tag{7}$$

[53]

$$c_{P,l} = 1010 + 1.554 T_{in} \tag{8}$$

The fluid properties used in this study come from the manufacturer's datasheet. Alternate sources such as National Institute of Standards and Technology (NIST) REFerence fluid PROPerties (REFPROP) could produce different fluid property results. A 1 % change in the fluid properties resulted in a 1 % change in the mass flux. A 1 % change in the fluid properties had a maximum impact of 3.2 % on the single-phase heat fluxes. The two-phase heat fluxes were affected by a maximum of 2 %. The impact of using a different source for the fluid's properties was thus determined not to affect the results and trends observed.

Table 3
Absolute uncertainties of the input parameters.

Parameter	Maximum relative error	Maximum absolute error
Thermocouple temperature (T)		± 0.14 °C
Infrared camera temperature (T_h)		± 0.18 °C
Heat absorbed ($\dot{Q}$)		± 0.61 W
Channel length (L)		± 0.01 mm
Channel internal width (W)		± 0.01 mm
Channel internal height (H)		± 0.01 mm
Distance from the inlet (z)		± 0.09 mm
Inclination (β)		± 1°
Liquid density (ρ_l)		± 0.37 kg/m^3
Voltage (U)	0.5 %+0.2 V (at resolution)	0.7 V
Current (I)	1 %+1 mA (at resolution)	1.4 mA
Volumetric flow rate ($\dot{V}$)	1 %	2 ml/h
Mass flux (G)	0.41 %	0.16 kg/m^2•s
Effective heat flux ($\dot{q}$)	1.6 %	0.5 kW/m^2

4.3. Uncertainty analysis

Table 3 presents the uncertainties of measured values and calculated output parameters. The uncertainties of each value were based on the method presented by Moffat [54], where uncertainty propagation was used. This method uses absolute uncertainties for directly measured values such as temperature, pressure, and relative humidity and relative uncertainties for output parameters like the heat flux. The maximum uncertainties of all parameters are also provided.

5. Inclination results

5.1. Validation

For the current one-sided heating channel with a hydraulic diameter of 909 μm and working with FC-72, prior experimental data from the literature for instability frequencies, instability duration or standard deviation of surface temperature is unavailable. 3 sets of experiments follow to validate the heat transfer calculation methodology, single-phase and two-phase inclination effects. Comparisons are made with experimental results from literature and theoretical predictions.

A previous flow boiling study conducted in the same facility by Wang et al. [55] was replicated so as to assess the replication accuracy, methodology and data reduction techniques of the measurements. In that study, the average heat transfer coefficient was determined for a channel with a width of 6 mm and height of 0.3 mm for a hydraulic diameter of 571 μm and an aspect ratio of 20 at similar mass and heat fluxes with the same FC-72 refrigerant. Reproduced results were within the uncertainty of the measurements [32,33], indicating the validity of the methods used in this study. The full comparison can be found in Vermaak, et al. [33].

A similar investigation of HFE-7100 flow boiling in a horizontal and vertical channel with a hydraulic diameter of 909 μm, aspect ratio of 10 at mass fluxes of 14 kg/m^2·s, 28 kg/m^2·s and 42 kg/m^2·s was completed by Widyatama et al. [56], also in the same experimental facility. This study looked at local heat transfer coefficients at various vapour qualities and heat fluxes ranging from 3.5 kW/m^2 to 24.3 kW/m^2. This test matrix was similar to the present study's work and allowed the horizontal data to be directly compared. The comparison in Fig. 4 shows good agreement between the two experimental data sets.

Vertical inclination data could not be compared as the heated surface temperature in the two-phase region dropped below the saturation temperature of FC-72, producing negative heat transfer coefficients, as is discussed in Section 5.2. Further comparisons were made between single-phase Nusselt numbers at an inclination of $\beta = 0°$ and $\beta = +90°$ and various sources from literature. Kim [57] showed that theoretical Nusselt numbers for single-phase fluids in ducts do not accurately represent the experimentally measured Nusselt numbers at low Reynolds numbers. Kim [57] observed that for deionised water, below a Reynolds number of 180, experimental Nusselt numbers were less than the theoretical predictions and above a Reynolds number of 180, the experimental Nusselt numbers were greater than the theoretical expected value. It was also found that when the channel aspect ratio increases the Nusselt number increases at the same Reynolds number, reducing the Reynolds number at which the theoretical Nusselt number switches from over to underpredicting the experimental measurement. Other authors have reported similar findings [58–60]. Two of the most widely used correlations for horizontal channels were developed by Morini [61], and Shah and London [62]. Morini [61] developed a 5th-order polynomial to predict the Nusselt number in a range of heating scenarios and channel aspect ratios. While Shah and London [62] produced a similar correlation. Vertical channels also have similar correlations developed by Barletta [63] and Hartnett and Kostic [64]. Both vertical channel correlations assumed a uniform heat flux and flow through rectangular channels.

These theoretical predictions are compared with the present study's results in Fig. 5. Other experimental data was selected and added to the comparison in Fig. 5. A summary of the experimental literature sources is given in Table 4. Each source in Table 4 shows several pieces of information, with the most important being the hydraulic diameter, aspect ratio and heating type. These should be compared with the values reported in Table 1. All experimental sources had rectangular channels and used deionised water as the heat transfer fluid.

Comparisons between the present study's data (20 kg/m^2•s and 40 kg/m^2•s) and the theoretical and literature sources at a horizontal inclination are shown in Fig. 5a. Comparisons at a vertical inclination are shown in Fig. 5b. Significantly more data is available at horizontal inclinations and for channels with aspect ratios similar to the present study. Good agreement is found between the present study's data and the literature sources when the hydraulic diameter and heating type are similar; for instance, when compared to Lee, et al. [66] and Wang et al. [65]. At smaller hydraulic diameters, like for Kim [57], the Nusselt number is lower than the present study's data. This observation is supported by Kim [57] findings, where an increased hydraulic diameter and aspect ratio typically increased the measured Nusselt number.

Comparisons with the present study's data (10 kg/m^2•s, 20 kg/m^2•s

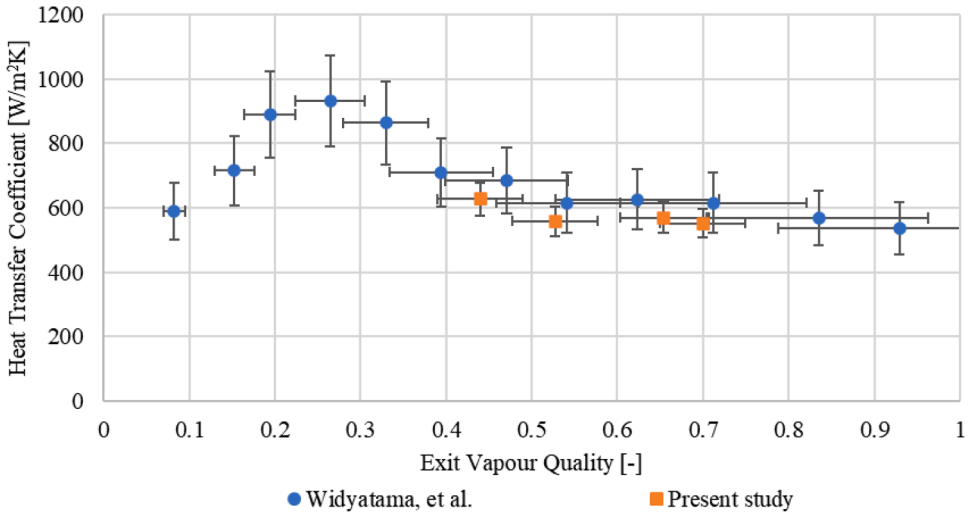

Fig. 4. Comparison between the present study's heat transfer coefficient and Widyatama, et al. [56] at a range of exit vapour qualities at a horizontal inclination and mass flux of 20 kg/m^2·s.

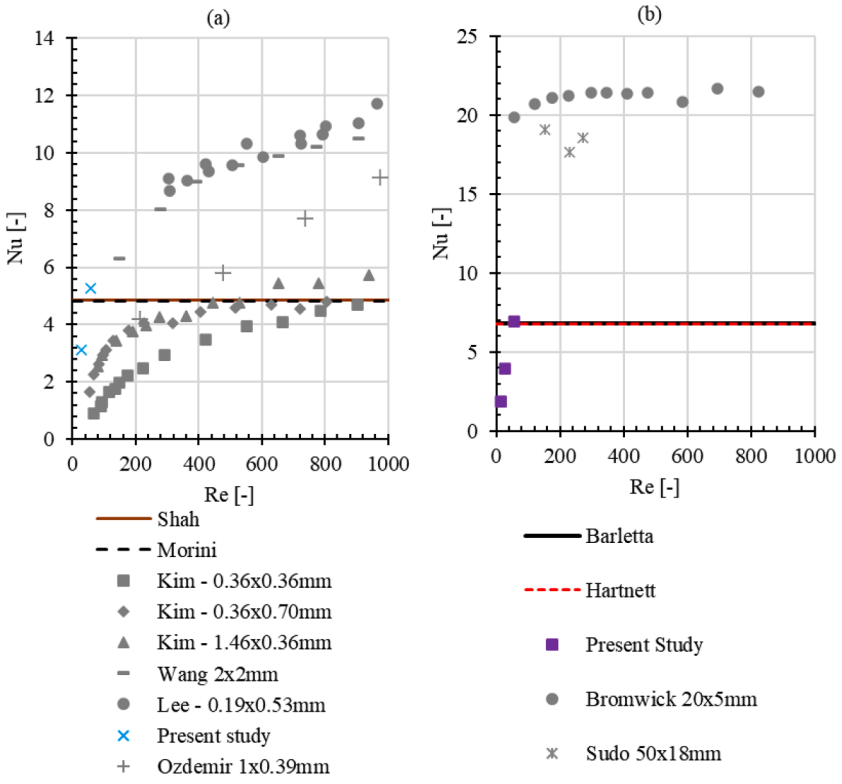

Fig. 5. Comparison of experimental results under single-phase heating with predictions from literature sources at (a) 0° at a mass flux of 20 kg/m^2•s and 40 kg/m^2•s and (b) 90° at a mass flux of 10 kg/m^2•s, 20 kg/m^2•s and 40 kg/m^2•s.

Table 4
Experimental conditions of reference sources.

Reference	Orientation	Number of channels	Geometry (*WxH* in μm)	Hydraulic diameter (μm)	Aspect ratio	Heating type	Fluid
Kim [57]	Horizontal	Multiple	363 × 363	363	1	Non-uniform	Deionised water
			367 × 703	482	0.5		
			1464 × 362	580	4		
Wang et al. [65]	Horizontal	11	2000 × 2000	2000	1	Uniform	Deionised water
Lee et al. [66]	Horizontal	10	534 × 2910	902	0.18	Non-uniform	Deionised water
Ozdemir et al. [67]	Horizontal	1	1000 × 390	561	2.6	Non-uniform	Deionised water
Bhowmik et al. [68]	Vertical	1	20,000 × 5000	8000	4	Non-uniform	Deionised water
Sudo et al. [69]	Vertical	1	50,000 × 18,000	26,470	2.7	Non-uniform	Deionised water

and 40 kg/m^2•s) and sources from literature were challenging for vertical channels. The vast majority of literature sources with channel sizes similar to the current study's data focused on Reynolds numbers greater than 1000 for uniformly heated circular channels for nuclear cooling applications. Little data is available in the range investigated in this study, and no data is available for FC-72. The literature sources from Table 4 have significantly larger hydraulic diameters, producing significantly higher Nusselt numbers. Instead, comparisons should focus on the theoretical predictions, where good agreement in Fig. 5b.

The comparisons from Vermaak et al. [33], Figs. 4, and 5 give confidence in the accuracy of the calculation method, the measured heat transfer rates for single and two-phase data, and the effect of inclination.

5.2. Steady state conditions

Steady-state conditions were defined by the absence of dynamic flow events, like two-phase mixing and rapid vapour motion towards the inlet, which is presented in Section 5.3. Examples of steady-state conditions are presented in this section for a wide range of mass fluxes, inclinations and heat fluxes. These cases best represent the influences described: negative inclined versus horizontal versus positively inclined and low versus high mass flux.

Typical steady-state flow patterns are shown in Fig. 6a and b at mass fluxes of 10 kg/m^2•s and 40 kg/m^2•s and a range of inclinations from $\beta = 0°$ to $+90°$ and $\beta = -20°$ to $+90°$ respectively, at their maximum respective heat flux case. The maximum heat flux was chosen because the nucleation site was closest to the inlet, the flow pattern was independent of heat flux, and the flow pattern took up the largest portion of the channel. Each figure shows the channel length below the final image in the set at 64 mm or 80 mm. The mass flux for each set is given above the figure, and the inclination and heat flux are given to the right of each image. Below each figure, the flow direction is shown from left to right in all cases. In each figure, the liquid phase, two-phase interface line and vapour phase are shown for the set's first image. The two-phase interface line is the most important of the annotations as it shows the number of bubbles and the size and shape of the large vapour slug. Where a clear nucleation site is observed, it has been indicated inside the purple circle. Regions in which the vapour slug is confined by the channel has been shown in green. All other regions should be considered unconfined.

At a mass flux of 10 kg/m^2•s, shown in Fig. 6a, two steady-state flow patterns are observed from the highspeed images at inclinations from $\beta = 0°$ to $+90°$. The first flow pattern presents with a single large vapour slug with no prominent nucleation site and a single two-phase interface line, observed at inclinations from $\beta = 0°$ to $+60°$ The vapour slug is also

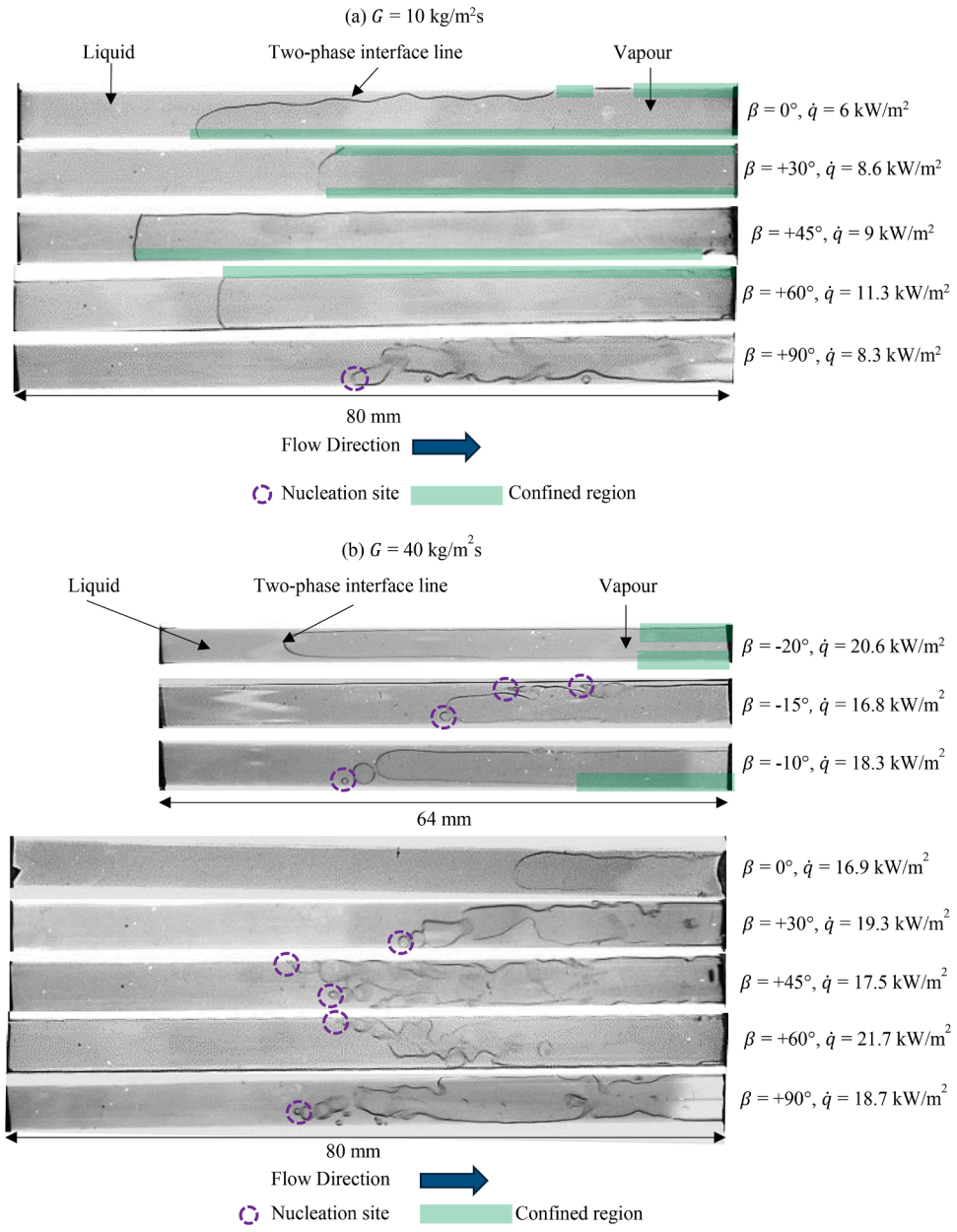

Fig. 6. Steady-state flow patterns at mass fluxes of (a) 10 kg/m^2•s and range of inclinations $\beta = 0°$ to 90° and (b) 40 kg/m^2•s and range of inclinations $\beta = -20°$ to 90°, at their corresponding maximum heat fluxes. The region with only liquid and vapour and the interface line between the two is indicated. The purple circles indicate nucleation sites, and the green shaded area indicates regions where the minichannel confines vapour slug growth. The flow direction is from left to right in all cases. The shorter length of $\beta = -20°$, $-15°$ and $-10°$ was due to channel breakages.

confined by at least one of the two side walls of the channel for most of its length. The second flow pattern is a churn flow pattern with multiple two-phase interface lines observed at $\beta = +90°$, i.e., vertical inclination. This churn flow pattern is identified with many bubbles of different volumes between the single-phase liquid region and the large vapour slug towards the channel's exit. The vapour slug is also unconfined and is fully detached from the side walls of the channel for most of the channel's length. The flow pattern in the churn case cannot be considered stratified flow because the stratified flow is observed once the Bond number exceeds 4.7 [70], significantly higher than 1.34 reported in Table 1 for the present study.

The steady-state flow patterns shown in Fig. 6b are for a mass flux of 40 kg/m^2•s and inclination angles ranging from $\beta = -20°$ to $+90°$ The same two flow patterns are again observed. With $\beta = -20°$, $-15°$, $-10°$ and 0° all having a single large vapour slug with a clear single two-phase interface line. At this mass flux, however, nucleation sites are clearly identifiable at $\beta = -15°$ and $-10°$ with a single bubble forming at the nucleation site, growing in size, detaching, moving downstream and coalescing with the vapour slug. Bubble growth, detachment and coalescence take two different forms. In $\beta = -15°$, the two upper nucleation sites produce a stream of small bubbles, which have most of their growth moving down the channel. The other nucleation site at $\beta = -15°$ (at the most upstream position) and the one observed in $\beta = -10°$, have a maximum of two bubbles between the nucleation site and the vapour slug. The size of the bubbles is also significantly larger than those observed at the downstream nucleation site, which has a stream of smaller bubbles. The other type of flow pattern observed is again churn flow, at inclination angles from $\beta = +30°$ to $+90°$. Here, multiple two-phase interface lines denoting multiple bubbles along the length of the channel are observed with no clear vapour slug observed for most of the

channel's length. Importantly, the vapour slugs observed in Fig. 6b are not fully confined for most of the channel's length. The bulk liquid and vapour velocities increase at higher mass fluxes, leading to elevated liquid drag forces and interfacial shear stresses. The increased shear disrupts the stability of vapour slugs, causing them to break down into smaller dispersed bubbles rather than maintaining a single large confined slug [71,72]. This indicates a mass flux effect on the level of confinement, with an increase in mass flux reducing the portion of the channel that has vapour confinement.

Slug flow transitions to churn flow when the fluid's velocity increases [73]. The fluid's velocity component in this study primarily has two components. The first is attributed to the bulk fluid's motion, the mass flux. The second component is from the vapour buoyancy, which varies depending on the inclination. At a mass flux of 10 kg/m^2•s, the bulk fluid motion component of the velocity vector is a quarter of the vector at a mass flux of 40 kg/m^2•s. The second component, buoyancy, always acts in the vertical upward direction, i.e., directly in line with the bulk fluid motion for $\beta = +90°$. As inclinations decrease from $\beta = +90°$ to 0°, an increasing portion of the vector acts tangentially to the bulk fluid motion, thus contributing less to the total fluid velocity. The component of the buoyancy vector acting tangentially to the bulk fluid motion also promotes side-wall interactions, which may reduce the vapour's motion. These effects are illustrated in that churn flow is only observed at an inclination $\beta = +90°$ at a mass flux of 10 kg/m^2•s but across a wider range of positive inclinations ($\beta = +30°$ to $+90°$) at a mass flux of 40 kg/m^2•s.

Infrared images of a subset of cases from Fig. 6 are shown in Fig. 7. The chosen cases highlight the effect of inclination angle, flow pattern and mass flux. Three image pairs are presented, with each pair sharing the same temperature range. The colours in the image indicate heated surface temperatures from purple to blue (low temperatures), green to yellow (medium temperatures), and finally, red and white (maximum temperatures), with a scale bar included along the different figure pairs. Bubble location, nucleation site location, local fluid phase and the ease with which the vapour can exit a channel affect the heated surface temperature. Fig. 7a shows the effect of inclination by comparing $\beta = -20°$ with a horizontal channel, both with the same flow pattern, mass flux and similar heat flux. The shorter length of $\beta = -20°$ was due to channel breakages. Flow pattern effects are shown in Fig. 7b, where for $\beta = +45°$ a single vapour slug is observed at a mass flux of 10 kg/m^2•s, and a churn flow pattern is observed at 40 kg/m^2•s. Mass flux effects are shown in Fig. 7c where $\beta = +90°$ at a mass flux of 10 kg/m^2•s is compared to 40 kg/m^2•s when both cases have a churn flow pattern.

Fig. 7a shows a case where the heated surface temperature for $\beta = -20°$ and 0° are compared under similar parameters: same flow pattern (slug flow), same mass flux (40 kg/m^2•s) and similar heat flux (16.4 kW/m^2 and 16.9 kW/m^2). The temperature range in the images is linearly scaled from 25.0 °C to 133.0 °C. At the maximum heated surface temperatures, a super heat of 77.0 °C is achieved with near or full dry out conditions in this region. The maximum surface temperatures for $\beta = 0°$ is higher than for $\beta = -20°$ despite applying the same mass flux and similar heat flux. The higher maximum surface temperature is likely due to a higher exit vapour proportion for $\beta = 0°$ than for $\beta = -20°$ Although the exit vapour quality could not be measured directly, $\beta = -20°$ and 0° had a similar heat flux, but the surface area for $\beta = 0°$ was applied over a larger surface area (due to the longer heated length). This larger amount of heat transferred to the fluid likely produced a higher vapour proportion at the channel's exit. A compounding effect was that at an inclination of $\beta = -20°$, the liquid and vapour phases' buoyancy acted in the opposite direction to the flow direction, resulting in the higher buoyancy vapour phase exiting the channel at a slower rate than the lower buoyancy liquid phase. This mass transfer effect made it impossible to accurately calculate the local or exit vapour quality for $\beta = -20°$. However, it is plausible that the vapour trapped in the channel would move to the centre or top of the cross-section, resulting in liquid moving along the bottom heated surface at a rate greater than the bulk fluid flow rate at the inlet, moderately improving the heat transfer rate and reducing the maximum heated surface temperature achieved. However,

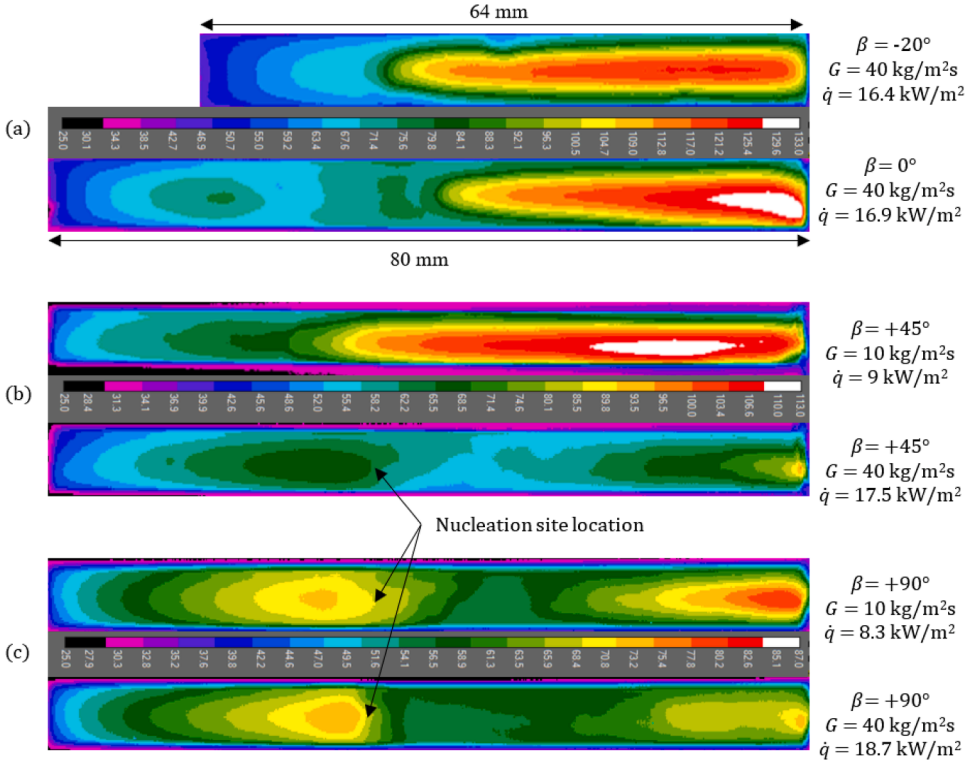

Fig. 7. Examples of steady-state temperature profiles at various inclinations, mass and heat fluxes. The Figure has 3 image pairs showing (a) inclination effects, (b) flow pattern effects, and (c) mass flux effects. The colours in the image scale from purple to blue (low temperatures), green to yellow (medium temperatures), and finally red and white (maximum temperatures).

temperatures exceeding 80.0 °C were achieved closer to the inlet and spanned a greater portion of the channel's length for $\beta = -20°$ than for $\beta = 0°$. This is primarily due to the mass transfer effect discussed above. At an inclination of $\beta = -20°$, the vapour's buoyancy component of the fluid velocity vector acts against the flow direction, slowing vapour removal from the channel, producing a large region with temperatures greater than 80.0 °C. The larger proportion of the channel at elevated temperatures is typical of negative inclinations and is one of the key challenges for these cases at low mass fluxes.

At an inclination of $\beta = +45°$, a single large vapour slug is observed at a mass flux of 10 kg/m^2•s, while a churn flow pattern is observed at a mass flux of 40 kg/m^2•s. The surface temperature maps shown in Fig. 7b show the influence of flow patterns. The heat flux ranges for the two flow patterns do not overlap, but the maximum heat flux tested at each mass flux was used to minimize the effect of heat flux on the results (9.0 kW/m^2 and 17.5 kW/m^2). Flow patterns were also the most consistent at the highest heat fluxes tested in the range. In the two flow pattern cases, the surface temperature increases to around 65.0 °C in the single-phase region. Once in the two-phase region, the surface temperature in the single vapour slug case continues to increase, reaching a maximum of over 110.0 °C close to the exit. At the maximum heated surface temperatures, a super heat degree of 54.0 °C is achieved with near dry-out conditions in this region. In the churn flow pattern case, the surface temperature decreases to the fluid's saturation temperature T_{sat} before increasing to a maximum of less than 100.0 °C, close to the channel's exit. The churn flow pattern supplies greater steady-state turbulent mixing in the two-phase region, improving the heat transfer rate by disrupting any thermal boundary effects on the heated surface. In the slug flow pattern case, liquid or vapour on the heated wall will be heated to temperatures greater than the saturation temperature if not replaced. The mixing associated with churn flow minimises the fluid temperature at the fluid-wall interface, promoting high heat transfer rates and preventing the heated surface temperature from rising. This mixing results in the surface temperature in the churn flow case reducing by up to 20.0 °C in the two-phase region compared to the peak measured just before the nucleation site.

Fig. 7c presents infrared temperature profile images of a channel at an inclination of $\beta = +90°$ at mass flux of 10 kg/m^2•s to 40 kg/m^2•s. At the maximum heated surface temperatures, a super heat of 28.0 °C is achieved with full dry out conditions not expected in this region. As in Fig. 7b, the maximum heat flux in the range was tested. A churn flow pattern was observed at both mass fluxes tested due to the high fluid velocity. The nucleation site locations are similar, and the surface temperatures after the nucleation site drop to close to or below the fluid's saturation temperature T_{sat}. Most heat transfer coefficient calculations in minichannels assume a uniform temperature in a cross-section, and the bulk fluid temperature after the nucleation site is assumed to be the saturation temperature. This assumption is invalid in this case as it would lead to negative heat transfer coefficients being calculated in the two-phase region due to the surface temperature dropping below 56.0 °C. It is plausible that the reduction in temperature below the saturation temperature is caused by the full cross-section of the channel not having reached saturation conditions and the vapour's buoyancy allowing it to exit the channel, keeping the primarily sub-cooled liquid at the fluid-wall interface, benefiting microelectronic cooling.

The observations above show that mass flux and inclination can produce significantly different steady-state flow patterns. These flow patterns, in turn, significantly affect the heated surface's temperature. Churn flow is the most desirable flow pattern observed, producing the lowest peak and average heated surface temperatures. Flow instability can disrupt these steady-state patterns, which is discussed in the following sections, starting with Section 5.3, which presents the types of flow instability events observed.

5.3. Flow instability identification

In this study, mild pressure-drop oscillation is used interchangeably with minor reverse and was defined as vapour front motion of between 1 % and 10 % of the channel's heated length towards the inlet without a flow pattern change in the two-phase region. While severe pressure-drop oscillation is used interchangeably with major reverse and is defined as vapour front motion of more than 10 % of the channel's heated length towards the inlet, accompanied by a flow pattern change in the two-phase region from slug flow to churn flow, examples of each flow pattern are presented in Section 5.2 above. Flow instability could change the steady-state flow pattern from slug flow to churn flow. These flow pattern changes could occur due to major reverse flow (severe pressure-drop oscillation) or occur in isolation. A flow pattern transition in the two-phase region from slug flow to churn flow without a reverse flow precursor is referred to as a two-phase mixing event in this study. High-speed images of minor (mild pressure-drop oscillation) and major reverse flow (severe pressure-drop oscillation), as well as two-phase mixing events are presented and defined in previous published work by the authors [32].

Fig. 8 shows a major reverse flow (severe pressure-drop oscillation) and a two-phase mixing event in Fig. 8a and b, respectively. The two events presented were for a channel with an inclination of $\beta = +60°$, mass flux of 40 kg/m^2·s and heat flux of 18.0 kW/m^2. The bulk fluid motion is from left to right, and the timestep is given on the left side of each image. The images selected are the ones that most accurately represent the instability type. The areas with two-phase mixing are indicated in purple, the nucleation site location is given in black, the vapour front position is given in red, and areas with liquid droplets deposited between the vapour slug and the top wall of the minichannel are given in blue.

Fig. 8a has images from 4 timesteps for a channel at $\beta = +60°$ with a mass flux of 40 kg/m^2•s and a heat flux of 18.0 kW/m^2. In the first image at +0 ms, major reverse flow (severe pressure-drop oscillation) is initiated, with two-phase mixing observed within the purple-shaded area, and the vapour starts to move towards the inlet. In the second image, at +25 ms, the vapour reaches its most upstream position, moving 11 % of the channel's length L_h towards the inlet from the original nucleation site. The most upstream bubbles occupy a large proportion of the channel's width, and no nucleation site at this position is visible. At +45 ms, the vapour retreats back towards the original nucleation site. This retreating vapour slug is large and, in most cases, occupies a greater proportion of the channel's width than in previous timesteps and initiated a secondary two-phase mixing event. At +85 ms, the vapour had returned to its original position, with the same nucleation site remaining active. These observations were typical of all major reverse flow (severe pressure-drop oscillation) events. Minor reverse flow (mild pressure-drop oscillation) events presented similarly, with the only differences being that the distance the vapour front moved towards the inlet never exceeded 10 % of the channel's heated length, and no two-phase mixing event accompanied the reverse flow.

From Fig. 8b, a typical two-phase mixing event can be observed for a channel at $\beta = +60°$, a mass flux of 40 kg/m^2•s and a heat flux of 18.0 kW/m^2. Here, highspeed images at 6 timesteps are given. In the first images, a small region with two-phase mixing is observed. At +25 ms, +45 ms and +60 ms, the region experiencing two-phase mixing increases in size and moves towards the channel's outlet. At +65 ms and +70 ms, the two-phase mixing event has finished, but some liquid droplets are observed close to the channel's outlet located within the blue shaded area. These droplets slowly evaporate, decreasing in size, and coalesce with the vapour slug. Throughout the two-phase mixing event, the nucleation site and vapour front position remain within 1 % of their starting location, indicating that this event is independent of reverse flow.

One of the key differences between Fig. 8a and b is the upstream bubbles and vapour slug formation. In Fig. 8a, multiple large bubbles

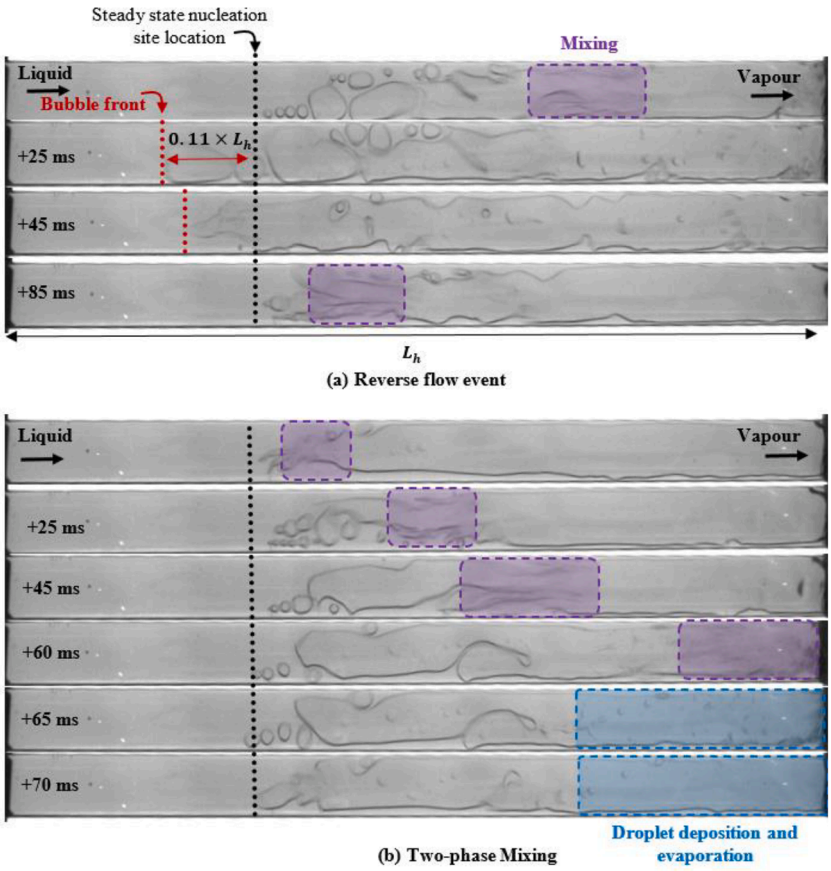

Fig. 8. A channel inclined at $\beta = +60^\circ$ with a mass flux of 40 kg/m^2•s and a heat flux of 18.0 kW/m^2 experiencing (a) major reverse flow (severe pressure-drop oscillation) and (b) two-phase mixing. The vertical black line indicates the bubble front, the purple shaded area indicates a region with two-phase mixing and the region indicated in blue indicates a region with droplet deposition and evaporation.

from at least 2 nucleation sites are observed, with some bubbles as large as 60 % of the channel's width upstream of the main vapour slug. When these bubbles coalesce with the main vapour slug, the confinement of the vapour slug by the channel's widths changes, creating intermittent, unconfined pockets containing only liquid. When a rapid phase change occurs in these pockets, the local high pressure pushes vapour towards the inlet and outlet, leading to reverse flow and two-phase mixing, a major reverse flow (severe pressure-drop oscillation).

The upstream bubbles in Fig. 8b are significantly smaller when they reach the vapour slug than those observed in Fig. 8a. The vapour slug changes confinement when these upstream bubbles coalesce with the vapour slug, but by narrowing the upstream portion of the vapour slug rather than creating a liquid pocket surrounded by vapour. When a rapid phase change occurs, the downstream vapour relieves the high pressure, changing the flow pattern from slug flow to churn flow (two-phase mixing). These differences in the upstream bubble sizes, shapes and position of the vapour slug are indicators of intermittent flow.

The primary difference between an event resulting in major reverse flow (severe pressure-drop oscillation) instead of minor reverse flow (mild pressure-drop oscillation) is the size of the high pressure created. As the size of the bubbles coalescing with the vapour slug increases, the size of the change in confinement also increases, producing larger liquid-only pockets. When the change in confinement is small, a rapid phase change will result in a smaller high pressure, enough to push vapour in the upstream and downstream direction but not high enough to change the flow pattern and produce two-phase mixing.

5.4. Instability maps

High-speed video footage from all experiments was analysed to determine if flow instability was observed, while the type of instability was determined using the classifications established in literature [7,8, 10–13] and [15]. The observational analysis was used to create instability maps, identifying the mass flux and heat flux combinations at which a single occurrence of major reverse flow (severe pressure-drop oscillation), minor reverse flow (mild pressure-drop oscillation), or two-phase mixing occurs.

Three instability maps are shown in Fig. 9, one for each mass flux: (a) 10 kg/m^2•s, (b) 20 kg/m^2•s and (c) 40 kg/m^2•s. Each sub-figure shows the channel inclination (°) on the x-axis, while the heat flux (kW/m^2) is shown on the shared y-axis. Major reverse flow (severe pressure-drop oscillation) is indicated by red squares, minor reverse flow (mild pressure-drop oscillation) with yellow circles and no reverse flow with green triangles. Two-phase mixing events are shown with solid black centres to any of these reverse flow indicators. All cases had at least one type of flow instability. Major reverse flow (severe pressure-drop oscillation) observations were always accompanied by minor reverse flow (mild pressure-drop oscillation) at the same inclination, mass flux and heat flux. Thus, a red square indicated both major (severe pressure-drop oscillation) and minor reverse flow (mild pressure-drop oscillation).

At a mass flux of 10 kg/m^2·s, in Fig. 9a, some inclination effects are observed. Positive inclination angles from $\beta = +30^\circ$ to $+90^\circ$ presented major reverse flow (severe pressure-drop oscillation) and two-phase mixing at all heat fluxes tested. On the other hand, major reverse flow (severe pressure-drop oscillation) was observed for a horizontal channel $\beta = 0^\circ$ at all heat fluxes tested except the highest one, where only minor reverse flow (mild pressure-drop oscillation) was observed. Two-phase mixing observations were heat flux dependent and only occurred at the maximum heat flux tested for $\beta = 0^\circ$. Hence, at the lowest mass flux tested, both inclination and heat flux played a role in the instability

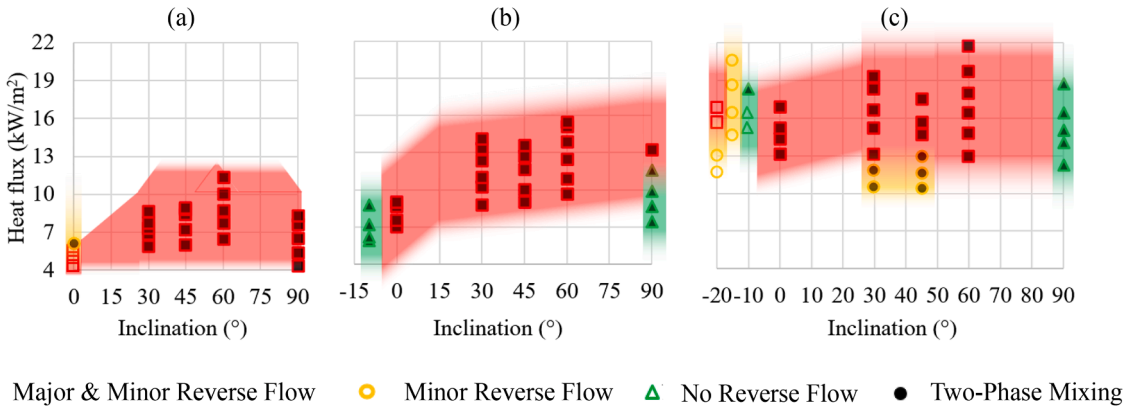

Fig. 9. Flow instability maps as major reverse flow (severe pressure-drop oscillation) in red squares, minor reverse flow (mild pressure-drop oscillation) in yellow circles and no reverse flow in green triangles with two-phase mixing events shown with solid black centres at mass fluxes of (a) 10 kg/m^2•s, (b) 20 kg/m^2•s, and (c) 40 kg/m^2•s at a range of inclinations) and heat fluxes.

maps.

At an increased mass flux of 20 kg/m^2•s, in Fig. 9b, allowed tests at an inclination angle of $\beta = -10°$ to be added to the analysis. $\beta = -10°$ experienced no reverse flow in the presence of two-phase mixing at all heat fluxes tested. Increasing the inclination angle to between $\beta = 0°$ and $+60°$, resulted in two-phase mixing and major reverse flow (severe pressure-drop oscillation) being observed for all heat fluxes. Further increasing the inclination to $\beta = +90°$ resulted in no reverse flow observed at heat fluxes below 13.0 kW/m^2, while two-phase mixing was present at all heat fluxes tested.

At a mass flux of 40 kg/m^2•s, in Fig. 9c, additional inclination angles of $\beta = -20°$ and $-15°$ could be tested. At these inclinations, no two-phase mixing was observed. Increasing the inclination to $\beta = -10°$ resulted in two-phase mixing being observed at only the highest heat flux tested. A clear inclination effect was observed with $\beta = -10°$ not having any reverse flow, $\beta = -15°$ having minor reverse flow (mild pressure-drop oscillation) at all heat fluxes, and $\beta = -20°$ having a transition from minor reverse flow (mild pressure-drop oscillation) to major reverse flow (severe pressure-drop oscillation) with an increase in heat flux to 15.5 kW/m^2. These reverse flow observations are attributed to the increased buoyancy force component acting in the direction opposite to the flow direction. Small local high-pressure regions created by pockets of liquid that rapidly changed phase to vapour were not large enough to force the vapour front towards the inlet at $\beta = -10°$ at the same heat flux. When the inclination was decreased to $\beta = -15°$, however, the component of the buoyancy force drawing the vapour towards the inlet was larger at the same heat flux. Combined with the small local high-pressure regions, this buoyancy force was large enough to result in minor reverse flow (mild pressure-drop oscillation). A further decrease in the inclination to $\beta = -20°$ allowed small local high pressure regions to cause major reverse flow (severe pressure-drop oscillation). Increasing the inclination from $\beta = -10°$ to $+0°$ resulted in two-phase mixing and major reverse (severe pressure-drop oscillation) flow being observed at all heat fluxes. This is due to buoyancy no longer playing a role and high pressures being eased by fluid motion to both the inlet and the outlet. Vapour was also no longer trapped in the channel, and the larger proportion of liquid resulted in the pressures resulting from rapid phase change becoming more intense. At inclinations between $\beta = 0°$ and $+90°$ two-phase mixing was observed at all considered heat fluxes. However, the prevalence of reverse flow, was more sensitive to inclination and heat flux. $\beta = 0°$ and $+60°$ exhibited major reverse flow (severe pressure-drop oscillation) at all heat fluxes tested. $\beta = +30°$ and $+45°$, transitioned from minor reverse flow (mild pressure-drop oscillation) to major reverse flow (severe pressure-drop oscillation) with an increase in heat flux. For $\beta = +90°$; however, reverse flow was not observed at any heat flux.

Negatively inclined channels (downward flow) exhibited reverse flow at heat fluxes higher than the ones presented in the instability maps, but such reverse flow resulted in vapour being deposited in the inlet plenum and the entire channel being filled by vapour, causing complete dry-out. These higher heat flux cases were not considered part of the flow boiling envelope assessed in this study and were omitted.

In summary, mass flux effects were observed mainly for $\beta = +30°$, $+45°$ and $+90°$ $\beta = +30°$ and $+45°$ had both two-phase mixing and major reverse flow (severe pressure-drop oscillation) observed at all heat fluxes tested at a mass flux of 10 kg/m^2•s and 20 kg/m^2•s, while only minor reverse flow (mild pressure-drop oscillation) was observed at heat fluxes below 13.2 kW/m^2 at mass flux to 40 kg/m^2•s for $\beta = +30°$ and $+45°$ The heat flux range decreased with major reverse flow (severe pressure-drop oscillation) as the mass flux increased at an inclination of $\beta = +90°$. Major reverse flow (severe pressure-drop oscillation) was observed at all heat fluxes tested at a mass flux of 10 kg/m^2•s, only at the highest heat flux tested at a mass flux of 20 kg/m^2•s, and was not observed at any heat flux at a mass flux of 40 kg/m^2•s. Negative inclinations presented with strong inclination effects at a mass flux of 40 kg/m^2•s. No reverse flow was observed at $\beta = -10°$, minor reverse flow (mild pressure-drop oscillation) was observed at all heat fluxes tested at $\beta = -15°$ and a transition from minor reverse flow (mild pressure-drop oscillation) to major reverse flow (severe pressure-drop oscillation) observed at heat fluxes above 13.0 kW/m^2 at $\beta = -20°$.

5.5. Pressure response observations

Instability maps effectively show the types of instability expected at the various testing conditions but do not indicate how often they occur. Continuous flow visualisation could determine the frequency of the instability events but is not practical due to memory storage constraints, the complexity of autonomous flow inspection, and the limitation of a transparent cooling channel requirement. An alternate way of detecting flow instability is to use the changes in pressure at the inlet and outlet.

Pressure changes/increases could occur due to flow instability, non-consequential flow phenomena, or system noise. A pressure threshold is required to differentiate between flow instability and other influences. Any pressure measured above this threshold would be indicative of flow instability. Determining this threshold requires comparing the flow instability detected with high-speed images.

A representative example of how the pressure correlates to the flow instability is shown with a set of 5 high-speed images in Fig. 10 for a channel with an inclination of $\beta = +60°$, mass flux of 10 kg/m^2•s and heat flux of 11.3 kW/m^2. For all cases, the bulk fluid motion in Fig. 10 is from left to right, indicated by the blue arrows. Flow reversal due to a major reverse flow (severe pressure-drop oscillation) event is indicated

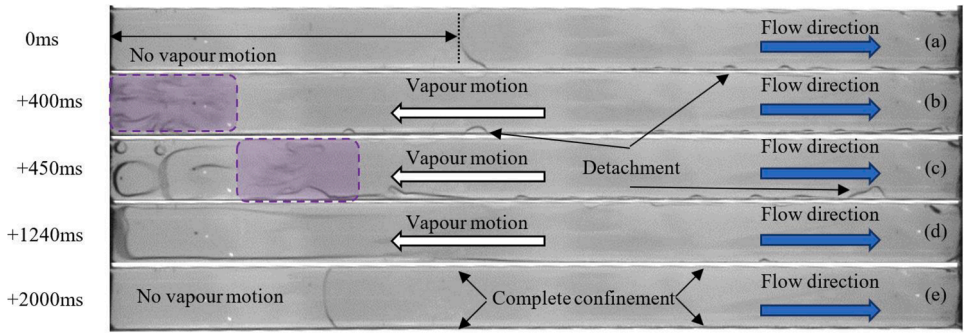

Fig. 10. Highspeed images of reverse flow for a channel inclined at $\beta = 60°$ at a mass flux of 10 kg/m^2•s and a heat flux of 11.3 kW/m^2 at (a) quasi-steady state at 0 s, (b) high mixing after vapour return from the 1st reverse flow event at +400 ms, (c) initiated secondary reverse flow event +450 ms (d) at the start of the 5th reverse flow event at +1240 ms and (e) with the formation of the new steady state position at +2000 ms.

by white arrows in Fig. 10b–d. Two-phase mixing is shown in the purple-shaded regions, and vapour detachment from the heated wall is indicated with black arrows. The images are a selection of key representative images. The entire set of images could not be shown as this set of instability events spanned for approximately 2 s. The characteristic pressure response for this set is shown in Fig. 11, and the temperature response for this instability event is shown in Fig. 15.

Fig. 10 shows the flow pattern changes due to multiple major reverse flow (severe pressure-drop oscillation) events. An initial steady-state profile is shown in Fig. 10a, where the vapour slug has small regions where the vapour slug is detached from the side wall. Flow reversal is shown in Fig. 10b-d, with a cascade of successive reverse flow events observed, with the vapour motion towards the inlet in each case exceeding 10 % of the channel's heated length. Many of these reverse flow events deposited vapour in the inlet plenum. Vapour deposited into the inlet plenum can re-enter when a stable flow pattern is observed and can trigger flow instability. Accompanying the reverse flow was two-phase mixing, shown in the purple region. During the major reverse flow (severe pressure-drop oscillation), multiple regions with vapour slug detachment from the heated wall are observed. In contrast, the vapour slug is completely confined by the width of the channel once the flow returns to stability, as shown in Fig. 10e.

The instability observed in Fig. 10 is more severe than that presented in Section 5.3 and extended for much longer than in Fig. 8. The case selected in Fig. 10 represented the most severe major reverse flow (severe pressure-drop-drop oscillation). The pressure response to this cascade of major reverse flow (severe pressure-drop oscillation) events is shown in Fig. 11, where the inlet and outlet pressure for a set of isolated two-phase mixing and major reverse flow (severe pressure-drop oscillation) events is shown in kPa on the *y*-axis as a function of time shown in seconds on the *x*-axis. The inlet pressure response is blue, and the outlet response is orange. Blue circles indicate reverse flow events, orange circles indicate two-phase mixing events, and red rectangles indicate major reverse flow (severe pressure-drop oscillation) events. The threshold pressures for this example were 5.9 kPa and 5.1 kPa for the inlet and outlet pressure, respectively.

Fig. 11 shows 5 inlet pressure measurements exceeding their instability threshold. In each case, at least one outlet pressure measurement exceeding its instability threshold is detected within 0.1 s of the inlet pressure measurement (6 outlet measurements in total). This combination of pressure measurements indicates 5 major reverse flow (severe pressure-drop oscillation) events, as is indicated in the red shaded regions. All other inlet pressure variations were below the threshold and could be ignored as they did not indicate flow instability. An additional 3 outlet pressure measurements exceeded the outlet instability threshold. These cases did not coincide with an inlet pressure exceeding its threshold and were indicative of a two-phase mixing event.

This analysis approach was generalised by first finding the mean inlet and outlet pressures. Next, a threshold pressure was calculated as the sum of the mean pressure and a pressure interval above the mean pressure (starting with 0.5 kPa). All pressure measurements were then compared to the threshold pressure to determine if they indicated an instability event. The time at which reverse flow and two-phase mixing occurred was then used to differentiate between minor (mild pressure-drop oscillation) and major reverse flow (severe pressure-drop oscillation) events, with a window of 0.2 s applied. If two-phase mixing and reverse flow occurred within 0.5 s of each other, the instability event was defined as major reverse flow. A MATLAB® script was used to calculate the reverse flow and two-phase mixing frequency for every 60 s long experiment (the entire dataset). The instability maps were then compared to the instability frequency results to evaluate if the correct threshold pressure was used. In cases such as $\beta = +90°$ at 20 kg/m^2•s, minor reverse flow (mild pressure-drop oscillation) was only observed for some heat fluxes, while other heat fluxes induced both minor (mild pressure-drop oscillation) and major reverse flows. The threshold pressure could then be adjusted in 0.1 kPa intervals until the instability

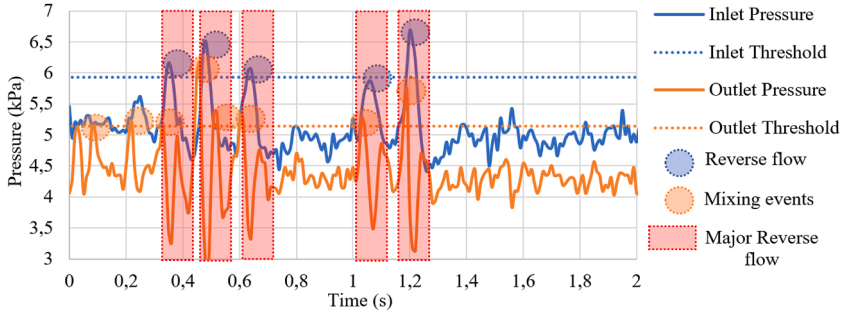

Fig. 11. An example of major reverse flow (severe pressure-drop oscillation) detection and isolated two-phase mixing events detection using inlet and outlet pressure transducers at an inclination of $\beta = +60°$, mass flux of 10 kg/m^2·s and heat flux of 11.3 kW/m^2. Representative highspeed images of reverse flow under different mass flux and heat flux conditions to those represented here can be found in Fig. 8.

frequency evaluation matched the instability maps. If major reverse flow (severe pressure-drop oscillation) and two-phase mixing occurred at all heat flux, then the approximate threshold was verified by comparing the calculated frequency with the highspeed video.

The number of detected instability events, n_P, above the threshold pressure, was then used in conjunction with the length of an experiment (60 s), Δt, to determine an instability frequency P_f in Hz.

$$P_f = \frac{n_P}{\Delta t} \tag{9}$$

Each experiment was repeated three times to get an average instability frequency for each inclination, mass flux and heat flux.

Other authors investigated instability frequency primarily in changes to the heated surface temperature and/or pressure-drop [74,75]. These studies found that for minichannels, the frequency in the surface temperatures and pressure-drop variations were typically less than 1 Hz. The focus of these studies differed from the present study, in that they focused on the thermal capacitance of the heat sink rather than variations in the heated surface temperature with each flow instability event.

5.6. Instability frequency

The methodology for determining the instability threshold is given in Section 5.5. This methodology was applied to the entire dataset, and the results of the two-phase mixing frequency are given in Fig. 12, and minor (mild pressure-drop oscillation) and major reverse flow (severe pressure-drop oscillation) are given in Fig. 14, respectively. Both figures have 3 subplots, giving results for each mass flux tested. In these subplots, the instability frequency is given on the shared y-axis in Hz and with a logarithmic scale, while the heat flux is given on the x-axis in kW/m^2 with a linear scale. Instability frequencies for stable cases where no instability was observed are shown in the figures at a frequency of 0.01 Hz. This ensures that stable cases also appear on the instability frequency plots and can be compared to inclinations with large instability frequencies.

At a mass flux of 10 kg/m^2•s in Fig. 12a, $\beta = 0°$ has two-phase mixing instability frequencies significantly lower than the other inclinations at all heat fluxes tested. Positive inclinations have instability frequencies typically ranging from 0.10 Hz to 1.10 Hz. At an angle of $\beta = +30°$, the instability frequency was largely independent of heat flux, with a frequency around 0.70 Hz measured for all of the considered heat fluxes. As the inclination angle increases to $\beta = +45°$, $+60°$ and $+90°$, a moderate increase in two-phase mixing frequency as heat flux increases is observed.

From Fig. 12b, at a mass flux of 20 kg/m^2•s, $\beta = -10°$ has two-phase mixing frequencies near 0.02 Hz and 0.03 Hz in all cases. For horizontal channels $\beta = 0°$, the two-phase mixing frequency increased from 0.50 Hz at the lowest heat flux tested to around 1.00 Hz for all other heat fluxes. Inclination has a substantial effect on the two-phase mixing frequency and is strongly dependent on heat flux when the inclination is further increased to between $\beta = +30°$ and $+90$. The instability frequency range for $\beta = +45°$, $+60°$ and $+90°$ was between 0.01 Hz and 2.00 Hz, while for $\beta = +30°$ the instability frequency range was between 1.00 Hz and 3.00 Hz.

The highest mass flux tested of 40 kg/m^2•s is shown in Fig. 12c. Negative inclination angles $\beta = -10°$, $-15°$ and - $20°$, had instability frequencies within a narrow band between 0.03 Hz and 0.08 Hz. The one outlier is the highest of the heat fluxes for $\beta = -20°$ reaching 0.30 Hz. This frequency equalled the lowest instability frequencies from the positive inclinations, ranging from 0.30 Hz to 3.50 Hz. $\beta = 0°$ had a decrease in the instability frequency with an increase in the heat flux to 0.30 Hz from 1.00 Hz. $\beta = +30°$, $+45°$ and $+60°$ were largestly independent of heat flux. $\beta = +90°$ had an increase in the instability frequency with heat flux from 0.30 Hz to 1.00 Hz. $\beta = +30°$ had the highest instability frequencies measured and ranged from 1.00 Hz to 3.50 Hz.

The instability frequency for $\beta = +30°$ was typically higher than any other inclination at all mass fluxes tested. The likely cause is the vapour front positions, as will be discussed in Fig. 13 for the 40 kg/m^2·s mass flux. As heat flux increases, the most upstream nucleation site position and associated vapour front position typically move towards the inlet as the liquid entering the channel reaches saturation temperatures progressively closer to the inlet [76]. Saturation conditions are required for nucleation sites to be activated and sustained. In the case of $\beta = +30°$, nucleation sites often remained at the same location with an increase in heat flux, significantly affecting the instability frequency observed for the 40 kg/m^2·s mass flux.

Fig. 13 presents highspeed images for a $\beta = +30°$ channel, at a mass flux 40 kg/m^2·s, and for the full range of heat fluxes tested, shown to the right of each image. In each case, the steady-state profile is shown with the fluid flow direction from left to right, the bubble front position indicated with a vertical red line, the nucleation site position indicated with a purple circle, and the channel length is given at the bottom of the

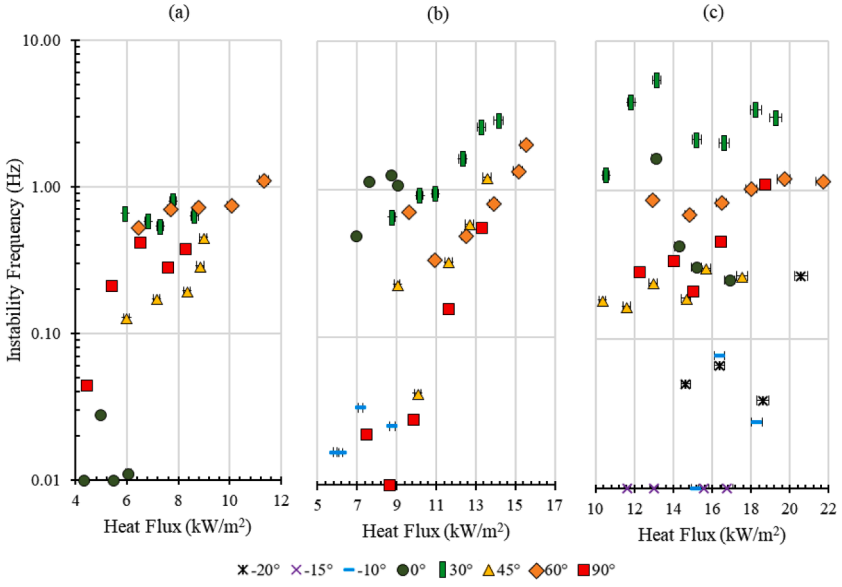

Fig. 12. Two-phase mixing instability frequency (Hz) at a mass flux in a log-normal scale for (a) 10 kg/m^2•s, (b) 20 kg/m^2•s and (c) 40 kg/m^2•s at all heat fluxes and inclinations tested.

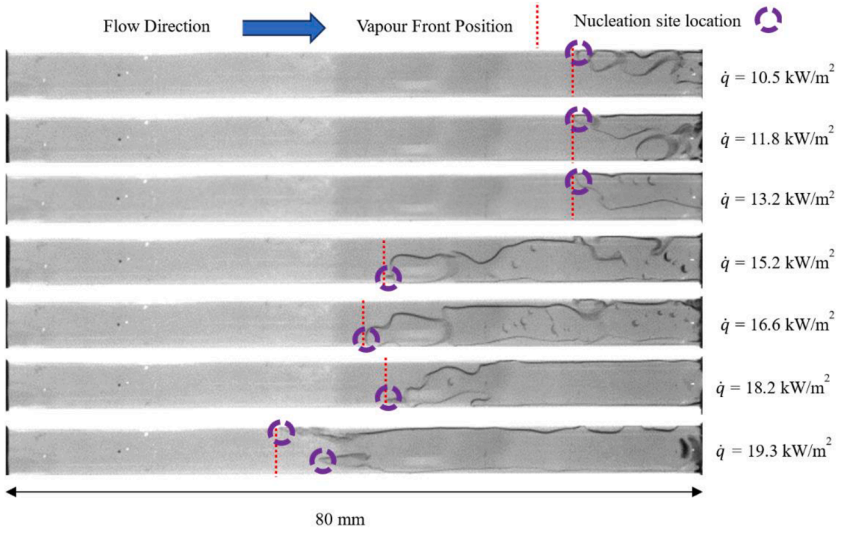

Fig. 13. Steady-state flow patterns at an inclination of $\beta = +30°$ and heat flux of 40 kg/m^2•s at various heat fluxes. Flow is from left to right in all images. The heat flux is given on the right of each image. Red dotted markers indicate the vapour front position and the purple circles indicate the nucleation site position.

Figure.

Fig. 13 shows that the vapour front position does not move incrementally closer to the inlet as heat flux increases, i.e., to the left side of the channel. The steady-state vapour front position for the first three heat fluxes tested (between 10.5 kW/m^2 and 13.2 kW/m^2) does not change. Further increasing the heat flux to 15.2 kW/m^2 did result in the vapour front position moving substantially closer to the inlet, with a new nucleation site becoming active. The steady-state vapour front's position remained largely unchanged between a heat flux of 15.2 kW/m^2 and 18.2 kW/m^2, while a further heat flux increase to 19.3 kW/m^2 resulted in the steady-state vapour front moving closer to the inlet.

Fig. 13 allows for the most upstream nucleation site(s) to be easily identified, while it is more difficult to identify whether the nucleation site from the previous heat flux case remains active. The nucleation site for a heat flux of 10.5 kW/m^2, 11.8 kW/m^2 and 13.2 kW/m^2 remains active for the higher heat flux cases. It is mostly clearly observed at 16.6 kW/m^2 but can be identified at 15.2 kW/m^2, 18.2 kW/m^2 and 19.3 kW/m^2. Most of the upstream nucleation sites observed for heat fluxes of

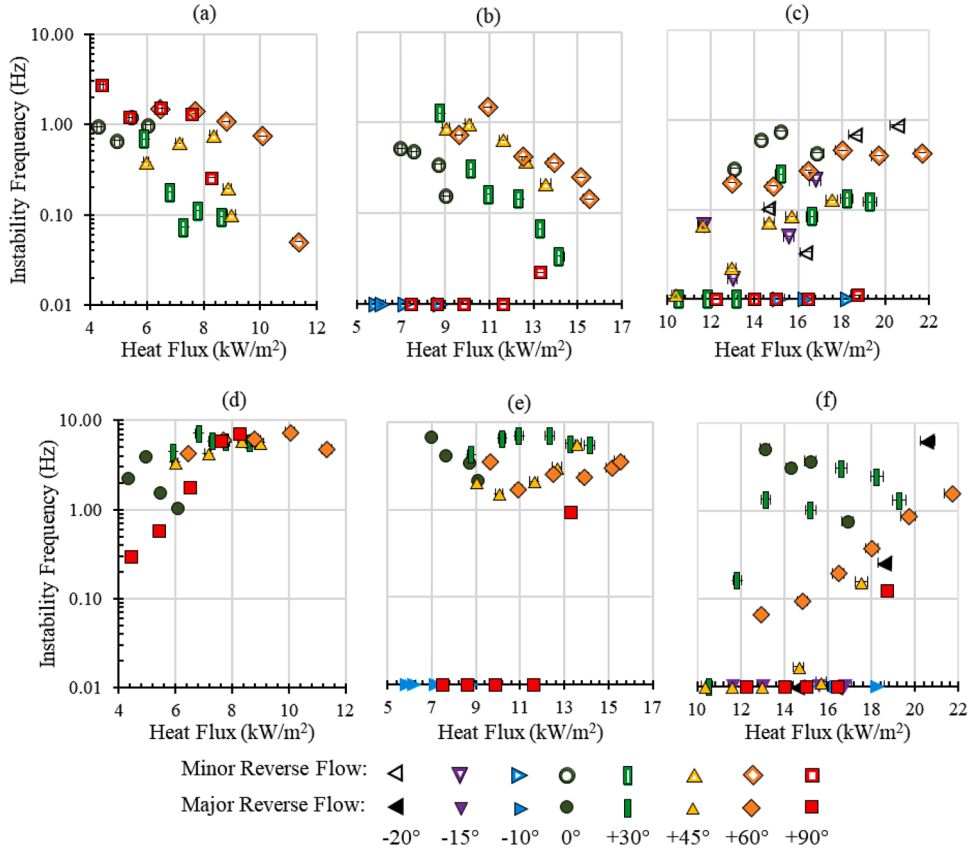

Fig. 14. Minor (mild pressure-drop oscillation) and Major reverse flow (severe pressure-drop oscillation) frequency at a mass flux of (a) 10 kg/m^2•s, (b) 20 kg/m^2•s and (c) 40 kg/m^2•s at all inclinations and heat fluxes.

15.2 kW/m^2, 16.6 kW/m^2, and 18.2 kW/m^2 are not clearly identifiable at a heat flux of 19.3 kW/m^2. This is because the nucleation site was located within the vapour slug region. A high-speed image taken from the side (rotated 90° about the flow path) would be needed to identify this nucleation site. However, due to the observations discussed for the nucleation site from 10.5 kW/m^2, 11.8 kW/m^2 and 13.2 kW/m^2, these nucleation sites are expected to remain at the same location.

The instability frequency measurement's change with heat flux in Fig. 12c correlates to the nucleation site position shown in Fig. 13. The instability frequency increases when the heat flux increases, and the nucleation site position remains unchanged. Then, the instability frequency decreases when the nucleation site position moves to the inlet with a further increase in the heat flux. These observations show that the nucleation site position significantly affected the two-phase mixing frequency.

In addition to two-phase mixing, as earlier reported in Fig. 10, minor reverse flow (mild pressure-drop oscillation) and major reverse flow (severe pressure oscillation) also ensue, depending on the working conditions. Fig. 14 presents then the flow instability frequency for minor reverse flow (mild pressure-drop oscillation) and major reverse flow (severe pressure-drop oscillation) at mass fluxes of (a) 10 kg/m^2•s, (b) 20 kg/m^2•s and (c) 40 kg/m^2•s at the different inclination angles studied. A shared legend is below Fig. 14, which uses similar symbols for each inclination but with minor reverse flow (mild pressure-drop oscillation) represented with hollow shapes, while major reverse flow (severe pressure-drop oscillation) is represented with solid shapes.

Fig. 14a and d shows that heat flux substantially affected the reverse flow frequency at the lowest mass flux of 10 kg/m^2•s. An increase in the heat flux produced a higher major reverse flow (severe pressure-drop oscillation) frequency and decreased minor reverse flow (mild pressure-drop oscillation) frequency for positively inclined channels. In the case of major reverse flow, an increase from 3.00 Hz to 7.00 Hz is reported for intermediate inclinations $\beta = +30°$, $+45°$ and $+60°$ while a greater increase is observed for $\beta = +90°$ from 0.30 Hz to 7.00 Hz. At an inclination angle of $\beta = 0°$, major reverse flow (severe pressure-drop oscillation) frequency increases from 2.00 Hz to 4.00 Hz and then decreases to 1.00 Hz as the heat flux increases further. At a mass flux of 10 kg/m^2•s, the inlet fluid momentum is low; thus, as flow boiling becomes more vigorous at higher heat fluxes, there is a decrease in the minor reverse flow (mild pressure-drop oscillation) frequency in favour of major reverse flow (severe pressure-drop oscillation) frequency.

Increasing the mass flux to 20 kg/m^2•s reduced the number of inclinations with clear heat flux effects on the instability frequencies, reported in Fig. 14b and e. At negative inclination angles $\beta = -10°$, no reverse flow was found at all heat fluxes tested. $\beta = 0°$, however, has major reverse flow (severe pressure-drop oscillation) frequencies as high as 8.00 Hz and minor reverse flow (mild pressure-drop oscillation) as high as 0.80 Hz. Both these reverse flow types decreased as heat flux increased. $\beta = +30°$ had no clear major reverse flow (severe pressure-drop oscillation) dependence on heat flux but typically had the highest frequency of all the inclinations. However, minor reverse flow (mild pressure-drop oscillation) decreases as heat flux increases. At larger inclination angles of $\beta = +45°$ and $+60°$, an increase in the major reverse flow (severe pressure-drop oscillation) frequency is reported as heat flux increases, while minor reverse flow (mild pressure-drop oscillation) frequency typically decreases with heat flux. $\beta = +90°$ only had reverse flow observed at the highest heat flux tested, with more data required to draw definitive conclusions about a heat flux dependence. However, this observation shows an inclination effect with negative inclinations and vertical upwards flow having little reverse flow, compared with the horizontal and intermediate positive inclinations.

At the highest mass flux studied of 40 kg/m^2•s, heat flux has little effect on the instability frequency at many inclinations, as reported in Fig. 14c and Fig. 14f. Clear heat flux effects are, however, observed at inclinations of $\beta = -20°$, $0°$, $+30°$ and $+60°$ At an inclination of $\beta = -20°$, the major reverse flow (severe pressure-drop oscillation) frequency increases from 0.30 Hz to 6.30 Hz between a heat flux of 18.0 kW/m^2 and 20.6 kW/m^2, while further increases in heat flux resulted in complete dry-out and could not be tested as was discussed in Section 3.2. $\beta = 0°$ had a decrease in the major reverse flow (severe pressure-drop oscillation) frequency as the heat flux increased. At the horizontal inclination of $\beta = 0°$, a nucleation site at the centre of the channel alternated between being active and inactive, with major reverse flow (severe pressure-drop oscillation) occurring with each reactivation of the upstream nucleation site. As the heat flux increases, the fluid reaches saturation temperature closer to the inlet, allowing the nucleation site (at the same upstream location for all heat fluxes) to remain active for longer, decreasing the number of reactivations and hence the major reverse flow (severe pressure-drop oscillation) frequency. $\beta = +30°$ had a vapour front position effect on the minor reverse flow (mild pressure-drop oscillation) and major reverse flow (severe pressure-drop oscillation), as was observed in Fig. 12 and explained in Fig. 13. A large increase in the major reverse flow (severe pressure-drop oscillation) frequency is observed when the heat flux increases from 11.8 kW/m^2 to 13.2 kW/m^2, when the vapour front position remains unchanged. Further increasing the heat flux, activities nucleation sites further upstream, decreasing the instability frequency. A further increase in the major reverse flow (severe pressure-drop oscillation) from 1.00 Hz to 4.00 Hz at a heat flux of 19.3 kW/m^2 is followed by a decrease with a further increase in the heat flux. Lastly, at an inclination of $\beta = +60°$, the minor reverse flow (mild pressure-drop oscillation) frequency stays within a tight band from 0.07 Hz to 0.40 Hz, while a larger major reverse flow (severe pressure-drop oscillation) frequency increases from 0.06 Hz to 2.00 Hz was observed. At an inclination of $\beta = +90°$, both the major reverse flow (severe pressure-drop oscillation) and minor reverse flow (mild pressure-drop oscillation) instability frequencies were low, at 0.01 Hz, with no heat flux effect observed.

As introduced above, heat flux, mass flux, and inclination affected both minor (mild pressure-drop oscillation) and major reverse flow (severe pressure-drop oscillation) frequencies. The minor reverse flow (mild pressure-drop oscillation) frequency decreased as heat flux increased at a mass flux of 10 kg/m^2•s and 20 kg/m^2•s for most inclinations. At a mass flux of 40 kg/m^2•s, *minor* reverse flow (mild pressure-drop oscillation) frequency for all channels was largely unaffected by heat flux. Major reverse flow (severe pressure-drop oscillation) frequency's dependence on heat flux and mass flux was inclination-dependent. $\beta = -20°$ at a mass flux of 40 kg/m^2•s had an increase in the major reverse flow (severe pressure-drop oscillation) frequency as heat flux increased, while $\beta = 0°$ had a decrease in the major reverse flow (severe pressure-drop oscillation) frequency as heat flux increased at all mass fluxes. At the same time, positive inclinations had no heat flux effect on the major reverse frequency at a mass flux of 10 kg/m^2•s and 20 kg/m^2•s, while an increase in the major reverse flow (severe pressure-drop oscillation) frequency was observed with an increase in heat flux at a mass flux of 40 kg/m^2•s. Conversely, $\beta = +90°$ had an increase in the major reverse flow (severe pressure-drop oscillation) frequency at a mass flux of 10 kg/m^2•s, while no heat flux effect was observed at a mass flux of 20 kg/m^2•s and 40 kg/m^2•s due to no major reverse flow (severe pressure-drop oscillation) occurring. The major reverse flow (severe pressure-drop oscillation) and minor reverse flow (mild pressure-drop oscillation) frequency typically decreased as inclination increases from $\beta = 0°$ to $+90°$ This reduction in instability frequency is attributed to a larger proportion of the vapour's buoyancy force component acting in the same direction as the bulk fluid's direction. At higher inclinations, larger local high pressure would be required to produce major reverse flow (severe pressure drop oscillation). Local high pressures that produced major reverse flow (severe pressure-drop oscillation) at less steep inclinations would produce minor reverse flow (mild pressure-drop oscillation), and those which previously produced minor reverse flow (mild pressure-drop oscillation) did not result in reverse flow.

5.7. Temperature profile observations

Flow instability effects presented in previously published work [32] showed that surface temperatures decrease when reverse flow or two-phase mixing occurs for horizontal channels. Fig. 15 emphasises those observations for channels at a range of inclinations with surface temperature profiles over a 2.00 s period with five major reverse flow (severe pressure-drop oscillations) events occurring between 0.30 s and 1.30 s. These major reverse flow (severe pressure-drop oscillation) events correspond to the high-speed images in Fig. 10 and as inlet and outlet pressures in Fig. 11 for a channel inclined at $\beta = +60°$ at a mass flux of 10 kg/m^2•s and a heat flux of 11.3 kW/m^2. The example given in Fig. 15 is the most intense 2.00 s period observed of all the cases tested. It was selected to show the potential surface temperature reductions that could be achieved.

Heated surface temperature profiles are shown in a three-dimensional form in Fig. 15a and a two-dimensional form in Fig. 15b. Fig. 15a presents temperature profiles for all timesteps across the 2.00 s span to demonstrate the heated surface temperature's evolution due to the major reverse flow (severe pressure-drop oscillations) events. Fig. 15b shows data from key selected time stamps, highlighting heated surface temperature improvements.

Fig. 15a shows the cross-sectionally averaged heated surface temperature for all timesteps with the time on the *x*-axis (s), the distance from the inlet (mm) on the *y*-axis, and the temperature on the *z*-axis (°C). The colour bar to the figure's right indicates the surface temperature, with red and white indicating high temperatures, while purple and blue indicate low temperatures.

Fig. 15b shows the cross-sectionally averaged heated surface temperature (°C) on the *y*-axis and the distance from the inlet from left to right (mm) on the *x*-axis. The axial distance from the inlet is split into two regions: the pre-nucleation region is the portion of the channel between the inlet and the nucleation site, and the post-nucleation region is between the nucleation site and the outlet. Two blue vertical dotted-dashed lines indicate the position in each region at which the largest surface temperature decrease is observed. Labels are provided to indicate the time of each temperature profile.

Fig. 15a presents cross-sectionally averaged temperature profiles for 50 timesteps over the span of 2.00 s. The decrease in heated surface temperature is observed by identifying colour changes and the *z*-axis values. Three distinct peaks are observed at around 20 mm, 50 mm, and 75 mm from the inlet. The peaks at 20 mm and 50 mm from the inlet decreases over time. The temperature at around 75 mm remains similar, with small variations observed up to the channel's exit.

Fig. 15b shows a subset of cross-sectionally averaged heated surface temperature profiles, highlighting the cooling effect of the successive major reverse flow (severe pressure-drop oscillation) events. Reverse flow cooled the pre-nucleation region, while two-phase mixing cooled the post-nucleation region. The surface temperature increased between 0 mm and 22 mm from the inlet, reaching a maximum pre-nucleation zone temperature at 22 mm before decreasing as it approached the nucleation site at 34 mm from the inlet. The temperature in the pre-nucleation region decreased with each successive reverse flow event. In this region, two-phase fluid moving towards the inlet can reduce heat

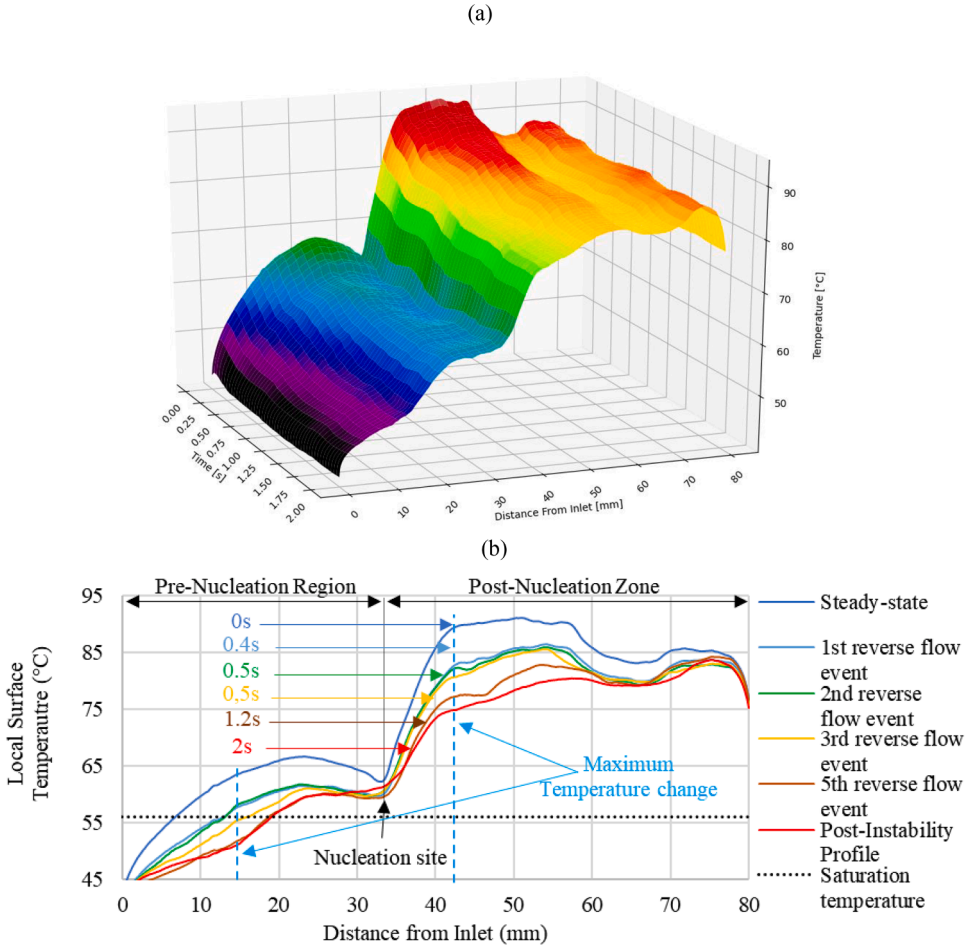

Fig. 15. An example of the change in the cross-sectional average heated surface temperature along the channel length from an initial steady-state profile after successive major reverse flow (severe pressure-drop oscillation) events. In this example, the inclination was $\beta = +60°$, mass flux was 10 kg/m^2•s and heat flux was 11.3 kW/m^2. (a) all timestamps between the initial steady-state and post-instability profile and (b) at key selected timestamps.

transfer performance and increase heated surface temperatures. However, in the cases above, the heat transfer performance was improved due to reverse flow because of changes in the fluid velocity. During steady-state, the fluid's velocity is low, allowing thermal gradients to form on the heated surface. Reverse flow forces the two-phase fluid to rapidly move across the heated surface, disrupting any thermal boundary layer that may have formed and significantly enhancing the forced convection heat transfer rate. Secondly, subcooled liquid entered the channel along with the two-phase fluid on re-entry. This turbulent re-entry with subcooled liquid at fluid temperatures lower than the saturated fluid improves the effective heat transfer rate, allowing the surface temperature to drop significantly, as shown in Fig. 15b.

This nucleation site was identified by observing the convex shape of all heated surface temperature profiles at 34 mm from the inlet and comparisons with the highspeed images in Fig. 10. This point delineates the transition point between the pre- and post-nucleation regions. The temperature at the nucleation site did not change during flow instability for the different reverse flow events, as bubble nucleation is a highly effective cooling method. Similar findings have been reported by Chen et al. [24]. The decrease in temperature close to the nucleation site has been observed in several other studies that tried to maximise the number of nucleation sites to further benefit from the phenomenon [77]. The superheat temperature required for boiling also decreases when more nucleation sites are active [78], typically due to increased surface roughness.

In the post-nucleation region shown in Fig. 15b, a sharp increase in the temperature is observed between the nucleation site and around 43 mm from the inlet, where the temperature remains constant until around 58 mm. Typically, the heated surface temperature decreases downstream from a nucleation site due to the bubble dynamics associated with the nucleation site. As the bubble formed, detached and grew before moving downstream and coalescing with the main vapour slug, a region with a reduced heated surface temperature was often observed. The results in Fig. 15b instead show that the nucleation site was within the vapour slug region, as is shown in Fig. 10. No region with bubble growth and free movement upstream of the vapour slug was observed. It should also be noted that the vapour slug was confined by the channel's width directly after the vapour front and nucleation site. This resulted in no liquid only region clearly in contact with the heated surface, resulting in a lower heat transfer rate. These two factors caused the rapid increase in the heated surface's temperature downstream of the nucleation site. The constant temperature between 58 mm from the inlet and the outlet is caused by a constant low heat transfer rate stemming from the confined vapour slug. This region did not experience dry-out. If full dry-out were achieved, the surface temperature would have exceeded 150.0 °C, as was observed at the highest heat flux cases, and would not have decreased further downstream where the level of confinement changed.

The successive reverse flow events produced a maximum pre-nucleation region heated surface temperature reduction of 14.1 °C from 64.2 °C (at 0.00 s) to 54.9 °C (at 1.20 s and 2.00 s), 15 mm from the inlet. A similar amount of cooling occurred in the post-nucleation region, where the temperature decreased by 15.0 °C from 99.8 °C (at 0 s) to 84.8 °C (at 2 s), 42 mm from the inlet. These temperature reductions are cases where the cooling effect from major reverse flow (severe pressure-drop oscillation) is maximised. The extent of the cooling is dependent on inclination, mass flux, and heat flux. Section 5.8 presents the typical improvement in the heat transfer rate for the full test matrix. This improvement considers the entire channel and does not differentiate between the pre- and post-nucleation regions, nor does it focus on the maximum improvements. This will result in a conservative estimate of the heat transfer improvement.

5.8. Instability assisted temperature reductions

The observations from Fig. 15 highlight the potential for large decreases in the heated surface's temperature after a major reverse flow (severe pressure-drop oscillation) instability. Previously published work quantified flow instability's effect on the heated surface temperatures at different rotations using heat transfer coefficients [32]. One key assumption for that calculation was that the bulk fluid temperature in a cross-section was uniform and that no buoyancy-driven mass transfer occurred. The first assumption is likely to be true in these experiments. Without buoyancy-driven mass transfer, the bulk fluid temperature in the two-phase region could be assumed to be the saturation temperature of the fluid, measured using the outlet thermocouple. The heated surface's temperature for positively inclined channels (upward flow) had sections in the two-phase region, where the temperatures were less than the saturation temperature, as is shown in Fig. 7. This temperature difference would suggest that heat flowed from the fluid to the heated surface (a negative heat transfer coefficient), which is thermodynamically infeasible. This approach thus deemed inappropriate for use in this study.

Heat transfer improvements in this section are thus presented as percentage heat flux improvement across the entire channel. This improvement is defined here as the change in the amount of heat the channel absorbed before and after an instability event occurred. The starting temperature was taken as the spatially averaged surface temperature at the time at which an instability event occurred. The reduction in temperature after flow instability, was the lowest spatially average surface temperature within 0.2 s after the start of the instability event. The effective heat flow into the channel $\dot{q}$ was then calculated using Eq. (2) by first considering the heat lost $\dot{Q}_0$ at both temperatures using Eq. (4) and the uniform heat flux input power $\dot{Q}_h$ using Eq. (3). This net heat flow was compared with the starting heat flow to get the percentage improvement.

The heat transfer improvements for two-phase mixing and minor (mild pressure-drop oscillation) and major reserve flow are shown in Figs. 16 and 17. In both figures, 3 subplots are included showing results at mass fluxes of (a) 10 kg/m^2•s, (b) 20 kg/m^2•s and (c) 40 kg/m^2•s. The *y*-axis is shared and indicates the heat transfer improvement as a percentage, and each subplot has a unique *x*-axis, denoting the effective heat flux in kW/m^2. The legend is shared between subplots and can be found below each figure, with Fig. 17 having one legend for both minor (hollow shapes) and major (solid shapes) reverse flow.

The heat transfer improvement increased with heat flux at a mass flux of 10 kg/m^2•s, as is shown in Fig. 16a, with the maximum heat transfer improvement measured at the maximum heat flux tested for all inclinations. The amount of cooling that can occur is limited by the difference between the heated surface temperature before instability and the minimum temperature the heated surface can achieve. The minimum temperature in the two-phase region is typically the saturation temperature of the two-phase fluid. The heated surface temperature increases during steady-state conditions, with the rate and maximum temperature that can be achieved determined by many factors, including the heat flux, steady-state flow pattern, and instability frequency. The rate at which the heated surface temperature increases during steady-state conditions increases with heat flux. Thus, a case with the same instability frequency could result in a larger cooling potential, as was observed for all inclinations. $\beta = 0°$ had heat transfer improvements that were significantly higher than the positive inclinations. This was caused by the maximum temperature that was achieved by the heated surface. Figs. 6 and 7 showed that the slug pattern produced surface temperatures significantly higher than the churn flow pattern cases under similar conditions. The inclinations in Fig. 16a all had the slug flow pattern, except for $\beta = +90°$ which had the churn flow pattern. Thus, the flow pattern was not the cause of the difference between the $\beta = 0°$ heat transfer improvement and those of the positive inclinations. Fig. 15 then showed that successive flow instability events can continually improve the heated surface temperature if the temperature is significantly above the saturation temperature or minimum temperature. When the instability frequency is low, in the case of $\beta = 0°$, the maximum surface

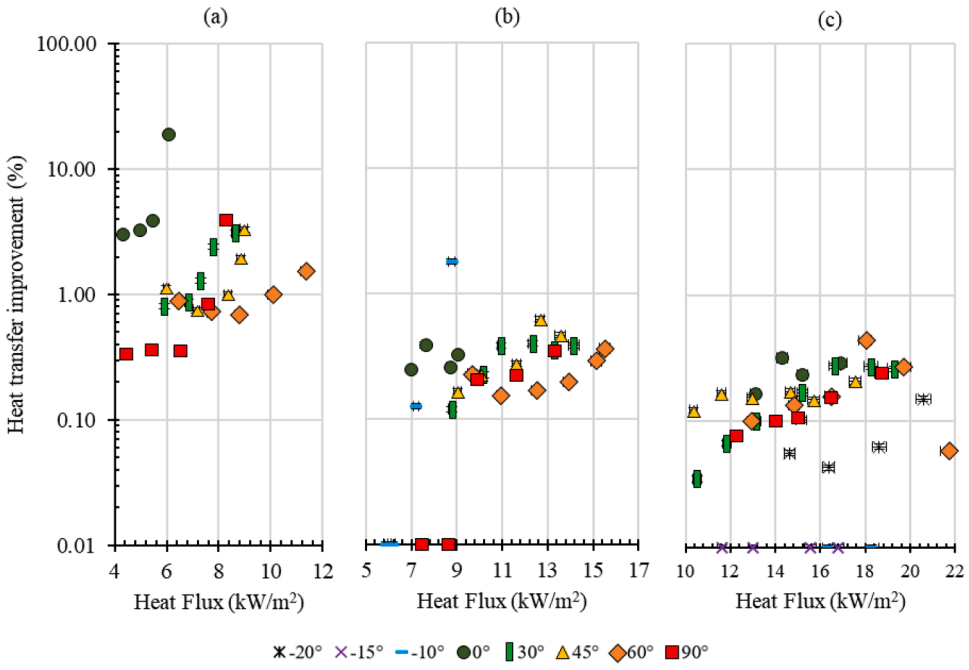

Fig. 16. Two-phase mixing heat transfer improvement as a function of effective heat flux at a mass flux of (a) 10 kg/m^2•s, (b) 20 kg/m^2•s and (c) 40 kg/m^2•s for the different inclination angles studied.

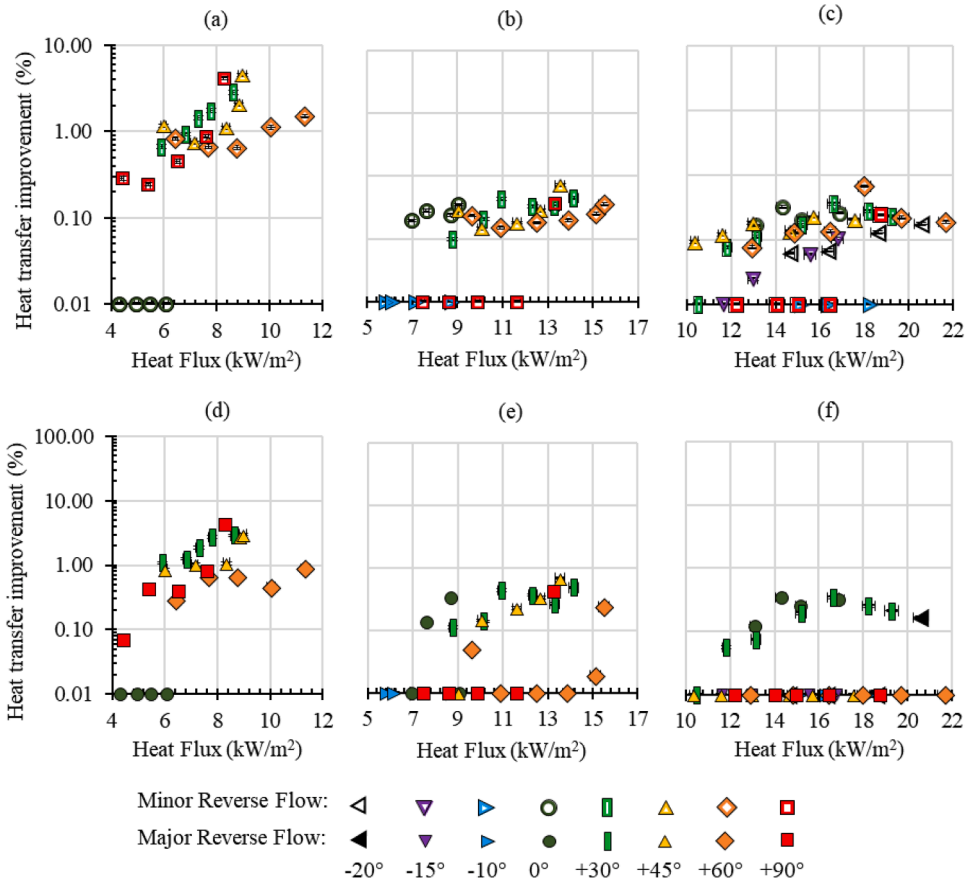

Fig. 17. Minor (mild pressure-drop oscillation) and Major reverse flow (severe pressure-drop oscillation) heat transfer improvement at a mass flux of (a) 10 kg/m^2•s, (b) 20 kg/m^2•s and (c) 40 kg/m^2•s for the different inclination angles studied.

temperature achieved was higher than the positive inclinations, allowing each instability event to produce a larger average heat transfer improvement.

The heat transfer improvement is typically lower at a mass flux of 20 kg/m^2•s, shown in Fig. 16b, than was reported at a mass flux of 10 kg/m^2•s. Heat flux effects are also only observed at an inclination of $\beta = -10^\circ$, where the heat transfer improvement increased from 0.10 % to 2.00 %. Fig. 12b shows that the instability frequency for $\beta = -10^\circ$ does not change significantly with an increase in heat flux. This results in an increasing cooling potential, as is exemplified by the results in Fig. 16b. However, Fig. 12b also shows that the horizontal and positive inclinations had instability frequencies increasing significantly with heat flux. This rapid increase in instability frequency resulted in the cooling potential (described above) remaining similar and a heat transfer improvement of around 0.20 % to 0.80 % measured for most cases.

At the highest mass flux studied of 40 kg/m^2•s, reported in Fig. 16c, modest heat transfer improvements below 1.00 % are reported. Some mild non-consequential heat flux effects are observed for $\beta = -20^\circ$, -30°, and $+90^\circ$ To understand the low heat transfer improvement and absence of significant heat flux effects, the flow patterns and resulting heated surface temperature profiles from Figs. 6 and 7 must be considered. The flow pattern for all positive inclinations was churn flow, which has a low cooling potential due to the natural mixing from the flow pattern, keeping the heated surface temperature similar to the saturation temperature of the fluid. $\beta = 0^\circ$ is an interesting case, as the flow pattern for these cases is slug flow and the instability frequency decreases as heat flux increases. These observations would normally suggest that the cooling potential should increase with heat flux; however, this is not the case because the major reverse flow frequency was often in the 2.00 Hz to 3.00 Hz range, as shown in Fig. 15c. This high major reverse flow (severe pressure-drop oscillation) frequency kept the cooling potential low by regularly reducing the surface temperature to at or near the saturation temperature. The $\beta = 0^\circ$ results will be further explored below. Negative inclinations have a low heat transfer improvement and low instability frequency, as shown in Fig. 15c. This low instability frequency, combined with the slug flow pattern shown in Fig. 6, produced high surface temperatures in Fig. 7. This high cooling potential did not result in a high heat transfer improvement because of the high vapour quality in the channel. With vapour trapped inside the channel, two-mixing had a relatively small liquid fraction in a cross-section, reducing the amount of cooling that could occur.

The major reverse flow (severe pressure-drop oscillation) and minor reverse flow (mild pressure-drop oscillation) heat transfer improvements are shown in Fig. 17. Fig. 17a and e shows the heat transfer improvement increasing for positively inclined channels as heat flux increases at a mass fluxes of 10 kg/m^2•s. This heat flux effect is most pronounced for $\beta = +30^\circ$, $+45^\circ$ and $+90^\circ$ with $\beta = +90^\circ$ having a change from 0.07 % up to 4.00 %, the maximum heat transfer improvement of any positive inclination. $\beta = 0^\circ$ on the other hand had a heat transfer improvement of up to 10 %, although no clear heat flux effect was observed. When comparing the difference between horizontal and positive inclinations, Figs. 6 and 7 show that flow pattern is not the cause of the difference as $\beta = 0^\circ$ to $+60^\circ$ had a slug flow pattern while $\beta = +90^\circ$ had a churn flow pattern. Fig. 14 shows that the major reverse flow (severe pressure-drop oscillation) and minor reveres flow frequencies (mild pressure-drop oscillation) were similar for all inclinations, ranging from 2.00 Hz to 10.00 Hz, and thus are not the cause of the difference in heat transfer improvement between the positive inclinations and $\beta = 0^\circ$ $\beta = 0^\circ$ achieved more than double the heat transfer improvement on average due to the low two-phase mixing frequency. The positive channel's cooling potential was lower because more two-phase mixing events occurred between each major reverse flow (severe pressure-drop oscillations) and minor reverse flow (mild pressure oscillations) event. $\beta = 0^\circ$ had a longer period of time without any instability event, allowing the cooling potential to increase further than for the positive inclinations.

Heat flux effects on the heat transfer improvement were absent or inconsistent at most inclinations at a mass flux of 20 kg/m^2•s in Fig. 17b and e. The heat transfer improvement for minor reveres flow frequencies (mild pressure-drop oscillation) was the same value for all heat fluxes tested. The heat transfer improvement for major reverse flow (severe pressure-drop oscillation) was not strongly correlated to heat flux. $\beta = +30^\circ$ and $+45^\circ$ had a small increase in the heat transfer improvement with heat flux. $\beta = +60^\circ$ had a unique relationship between the heat transfer improvement for major reverse flow (severe pressure-drop oscillation) and the heat flux. This inclination has a heat transfer improvement drop to very low levels between the minimum and maximum heat flux studied.

At the highest mass fluxes of 40 kg/m^2•s, heat flux and heat transfer improvement were not strongly correlated, as shown in Fig. 17c and f. Negatively inclined channels $\beta = -20^\circ$, $-15^\circ$and -10°, had a moderate heat transfer improvements increase with heat flux for minor reverse flow (mild pressure-drop oscillation), while no clear relationship between heat flux and major reverse flow (severe pressure-drop oscillation) was observed. Horizontal and positive inclinations had weak major reverse flow (severe pressure-drop oscillation) and minor reverse flow (mild pressure-drop oscillation) heat transfer improvement effects from heat flux. What was clear was the effect of inclination. Increasing the inclination to $\beta = 0^\circ$ and $+30^\circ$ resulted in major reverse flow (severe pressure-drop oscillation) heat transfer improvements of up to 0.30 %, while all other inclinations had an improvement of approximately 0.01 % (negligible). The minor reverse flow (mild pressure-drop oscillation) has a higher heat transfer improvement than the major reverser flow (severe pressure-drop oscillation) for $\beta = +45^\circ$ and $+60^\circ$ at a mass flux of 40 kg/m^{2}s. When first considering the post-nucleation region, the change in flow pattern from slug to churn flow results in the region having a small cooling potential. Thus, the major reverse flow does not substantially cool this region as the flow pattern already sufficiently cools it. Both reverse flow types reduce the heated surface temperature in the pre-nucleation zone. Major reverse flow (severe pressure-drop oscillation) deposits more vapour into the pre-nucleation zone than minor reverse flow. When this vapour reenters and moves downstream, it is expected to occupy a larger portion of the cross-section closer to the inlet than during minor reverse flow (mild pressure-drop oscillation). The result is vapour close to or in contact with the heated surface. This would reduce the amount of cooling that could occur, resulting in a poorer heat transfer performance. This effect is not observed at negative inclinations or $\beta = 0^\circ$ and $+30^\circ$, as the vapour would be more likely to move to the top of the channel, away from the heated surface, due to buoyancy.

6. Conclusion

This work reported on observations made about three types of flow instability: major reverse flow (severe pressure-drop oscillation), minor reverse flow (mild pressure-drop oscillation), and two-phase mixing. The instability types correspond with those identified in previous published work Qu et al. [11]. The type of instability observed in the instability maps was affected by inclination, mass flux and heat flux. Negative inclinations had the most pronounced inclination effect. $\beta = -10^\circ$ had neither minor (mild pressure-drop oscillation) nor major reverse flow (severe pressure-drop oscillation) observed, while minor reverse flow (mild pressure-drop oscillation) was observed at all heat fluxes for $\beta = -15^\circ$ and major reverse flow (severe pressure-drop oscillation) was observed at the highest heat fluxes tested at $\beta = -20^\circ$ $\beta = +90^\circ$ at a mass flux of 40 kg/m^2·s had an increase in the number of heat fluxes with major reverse flow (severe pressure-drop oscillation) or minor reverse flow (mild pressure-drop oscillation) as heat flux increased. An increase in heat flux typically resulted in more heat flux cases with major reverse flow (severe pressure-drop oscillation), like in the case of $\beta = -20^\circ$, $+30^\circ$ and $+45^\circ$ at a mass flux of 40 kg/m^2·s.

Highspeed image observations, summarised in the instability maps,

were compared with independent pressure transducer data to detect reverse flow and two-phase mixing. A threshold pressure was determined for each inclination and mass flux combination, and the results were compared with highspeed video footage to verify the chosen threshold. Inlet pressure measurements detected reverse flow, while outlet pressure measurements detected two-phase mixing events.

The two-phase mixing frequency was affected by inclination, mass flux and heat flux. At a mass flux of 10 kg/m^2·s, $\beta = +90^\circ$ had an increase in the two-phase mixing frequency from 0.04 Hz to 0.40 Hz. An order of magnitude or more increase in the two-phase mixing frequency was observed for $\beta = +30^\circ$, $+45^\circ$, $+60^\circ$ and $+90^\circ$ at a mass flux of 20 kg/m^2·s. A further mass flux increase to 40 kg/m^2·s resulted in no heat flux effect on the two-phase mixing frequency. Nucleation site location, however, was determined to have a large effect on the two-phase mixing frequency for $\beta = +30^\circ$, where the two-phase mixing frequency increased by up to 2.00 Hz when the heat flux increased by 1.7 kW/m^2, but the nucleation site location remained the same. A further increase in the heat flux and a nucleation site location moving closer to the inlet decreased the two-phase mixing frequency by up to 2.00 Hz.

Heat flux, mass flux, and inclination affected major reverse flow (severe pressure-drop oscillation) and minor reverse flow (mild pressure-drop oscillation) frequencies. Heat flux effects on the reverse flow frequency depended on mass flux and inclination. The minor reverse flow (mild pressure-drop oscillation) frequency decreased with increased heat flux at a mass flux of 10 kg/m^2•s and 20 kg/m^2•s while increasing the minor reverse flow (mild pressure-drop oscillation) frequency at 40 kg/m^2•s. The major reverse flow (severe pressure-drop oscillation) frequency's heat flux dependence was mass flux and inclination dependent. Negative, intermediate positive inclinations and $\beta = +90^\circ$ at a mass flux of 40 kg/m^2•s had up to an order of magnitude increase in the major reverse flow (severe pressure-drop oscillation) frequency as heat flux increased. $\beta = 0^\circ$ had a decrease in major reverse flow (severe pressure-drop oscillation) frequency as heat flux increased for all mass fluxes. Intermediate positive inclinations at a mass flux of 10 kg/m^2•s and 20 kg/m^2•s were unaffected by heat flux.

Due to vapour buoyancy, positive inclinations had an increased vapour velocity and higher shear stresses at the interfacial fluid liquid–vapour phase line. These effects promoted a change in the flow pattern with a breakdown of large vapour slugs into smaller bubbles, reducing the prevalence of major reverse flow (severe pressure-drop oscillation) and minor reverse flow (mild pressure-drop oscillations) events at higher inclinations. Additionally, the buoyancy force at positive inclinations greatly affected the vapour velocity, resulting in mass transfer effects driving vapour out of the channel and reducing heated surface temperatures. These observations were most pronounced at $\beta = +90^\circ$.

Instability-driven cooling reduces the heated surface temperature, benefiting microelectronic cooling applications, with multiple consecutive instability events having the potential for compounding cooling effects. The cooling effect was quantified using a heat transfer improvement. The maximum improvement that could be achieved was determined by the cooling potential. This potential was the difference between the heated surface temperature and the lowest temperature the heated surface could achieve. The lowest heated surface temperature that could be achieved was typically the saturation temperature of the fluid, while the maximum temperature depended on several factors, including the flow pattern and heat flux. The instability frequency was also shown to be very important to the maximum heat transfer improvement achieved, with $\beta = 0^\circ$ often having a heat transfer improvement up to 19 % higher than any other inclinations at the same heat flux and mass flux of (6 kW/m^2 and mass flux of 10 kg/m^2•s) due to the relatively low two-phase mixing frequency and slug flow pattern. Heat flux effects are typically mild, with similar heat transfer improvements expected at all heat fluxes tested in the range studied. High-frequency two-phase mixing, major reverse flow (severe pressure-drop oscillation) and minor reverse flow (mild pressure-drop oscillation) resulted in heat transfer improvements between 0.10 % and 1 % for the positive inclinations. The combination of high instability frequency at all mass fluxes and churn flow at higher mass fluxes resulted in a reduced but consistent cooling potential.

Microelectronic cooling can be optimised by employing positive inclinations with a mass flux of 40 kg/m^2·s. The high instability frequency and churn flow pattern reduce the heated surface temperature variance, promoting low steady-state surface temperatures and optimising microelectronic performance.

CRediT authorship contribution statement

Marius Vermaak: Writing – review & editing, Writing – original draft, Visualization, Validation, Methodology, Investigation, Formal analysis, Data curation, Conceptualization. **Jaco Dirker:** Writing – review & editing, Supervision, Resources, Methodology, Conceptualization. **Daniel Orejon:** Writing – review & editing, Supervision, Resources, Methodology. **Khellil Sefiane:** Writing – review & editing, Supervision, Software, Resources, Funding acquisition.

Declaration of competing interest

The authors declare that they have no known competing financial interests or personal relationships that could have appeared to influence the work reported in this paper.

Acknowledgments

This project has received funding from the European Union's Horizon 2020 research and innovation program under the Marie Skłodowska-Curie grant agreement No. 778104.

Data availability

Data will be made available on request.

References

[1] T. Zhang, T. Tong, J.-Y. Chang, Y. Peles, R. Prasher, M.K. Jensen, J.T. Wen, P. Phelan, Ledinegg instability in microchannels, Int. J. Heat. Mass Transf. 52 (25–26) (2009) 5661–5674.
[2] S. Szczukiewicz, N. Borhani, J.R. Thome, Two-phase flow operational maps for multi-microchannel evaporators, Int. J. Heat Fluid Flow 42 (2013) 176–189.
[3] G. Hetsroni, A. Mosyak, Z. Segal, G. Ziskind, A uniform temperature heat sink for cooling of electronic devices, Int. J. Heat. Mass Transf. 45 (16) (2002) 3275–3286.
[4] Ö. Çomaklı, S. Karslı, M. Yılmaz, Experimental investigation of two phase flow instabilities in a horizontal in-tube boiling system, Energy Convers. Manag. 43 (2) (2002) 249–268.
[5] D. Paul, S. Singh, S. Mishra, Stability analysis of parallel channels in flow boiling system: flow maldistribution and density wave oscillations, Chem. Eng. Sci. 212 (2020) 115316.
[6] L. Zhang, E.N. Wang, K.E. Goodson, T.W. Kenny, Phase change phenomena in silicon microchannels, Int. J. Heat. Mass Transf. 48 (8) (2005) 1572–1582.
[7] R. Muwanga, I. Hassan, R. MacDonald, Characteristics of flow boiling oscillations in silicon microchannel heat sinks, J. Heat Transf. 129 (10) (2007) 1341–1351.
[8] C.A. Chen, T.F. Lin, W.-M. Yan, Time periodic saturated flow boiling heat transfer of R-134a in a narrow annular duct due to heat flux oscillation, Int. J. Heat. Mass Transf. 106 (2017) 35–46.
[9] Y. Wang, K. Sefiane, R. Bennacer, Pressure drop and two phase flow during boiling of FC-72 in a high aspect ratio micro-channel, in: Proceedings of the 2010 14th International Heat Transfer Conference. 2010 14th International Heat Transfer Conference, 1, Washington, DC, USA, 2010, pp. 727–734. ASME.
[10] H. Jung, S. Lee, Mechanistic model to predict oscillating frequency of flow boiling in large length to diameter ratio micro-channel heat sinks, Int. J. Heat. Mass Transf. 215 (2023) 124473.
[11] W. Qu, I. Mudawar, Measurement and correlation of critical heat flux in two-phase micro-channel heat sinks, Int. J. Heat. Mass Transf. 47 (10) (2004) 2045–2059.
[12] M. Piasecka, K. Strąk, Influence of the surface enhancement on the flow boiling heat transfer in a minichannel, Heat Transf. Eng. 40 (13–14) (2019) 1162–1175.
[13] P. Balasubramanian, S.G. Kandlikar, Experimental study of flow patterns, pressure drop, and flow instabilities in parallel rectangular minichannels, Heat Transf. Eng. 26 (3) (2005) 20–27.
[14] S. Wang, H.-H. Chen, C.-L. Chen, Enhanced flow boiling in silicon nanowire-coated manifold microchannels, Appl. Therm. Eng. 148 (2019) 1043–1057.
[15] W. Qu, I. Mudawar, Measurement and prediction of pressure drop in two-phase micro-channel heat sinks, Int. J. Heat. Mass Transf. 46 (15) (2003) 2737–2753.

[16] L. Cheng, G. Xia, Fundamental issues, mechanisms and models of flow boiling heat transfer in microscale channels, Int. J. Heat. Mass Transf. 108 (2017) 97–127.
[17] T.A. Kingston, J.A. Weibel, S.V. Garimella, High-frequency thermal-fluidic characterization of dynamic microchannel flow boiling instabilities: part 2 – Impact of operating conditions on instability type and severity, Int. J. Multiph. Flow 106 (2018) 189–201.
[18] S. Lee, V.S. Devahdhanush, I. Mudawar, Investigation of subcooled and saturated boiling heat transfer mechanisms, instabilities, and transient flow regime maps for large length-to-diameter ratio micro-channel heat sinks, Int. J. Heat. Mass Transf. 123 (2018) 172–191.
[19] G. Hedau, M. Qadeer, N.P. Gulhane, R. Raj, S.K. Saha, On the importance of fluidic manifold design and orientation on flow boiling instability in microchannel heat sinks, Int. J. Heat. Mass Transf. 209 (2023) 124120.
[20] M.D. Clark, J.A. Weibel, S.V. Garimella, Impact of pressure drop oscillations and parallel channel instabilities on microchannel flow boiling and critical heat flux, Int. J. Multiph. Flow 161 (2023) 104380.
[21] S. Korniliou, C. Mackenzie-Dover, S. Harmand, G. Duursma, J.R.E. Christy, J. G. Terry, A.J. Walton, K. Sefiane, Local wall temperature mapping during flow boiling in a transparent microchannel, Int. J. Therm. Sci. 135 (2019) 344–361.
[22] Z. Jiang, Z. Ma, R. Yan, L. Zhang, W. Sun, S. Bu, L. Pan, Experimental study on the flow boiling oscillation characteristics in a rectangular multiple micro-channel, Exp. Therm. Fluid Sci. 109 (2019) 109902.
[23] X. Cheng, H. Wu, Impact of inlet subcooling on flow boiling in microchannels, Exp. Therm. Fluid Sci. 142 (2023) 110805.
[24] T. Chen, S.V. Garimella, Local heat transfer distribution and effect of instabilities during flow boiling in a silicon microchannel heat sink, Int. J. Heat. Mass Transf. 54 (15) (2011) 3179–3190.
[25] B. Maciejewska, M. Piasecka, A. Piasecki, The heat transfer and instabilities results during the onset of flow boiling in minichannels, in: E3S Web Conference 128, 2019 01016.
[26] R. Mastrullo, A.W. Mauro, L. Viscito, Flow boiling of R452A: heat transfer data, dry-out characteristics and a correlation, Exp. Therm. Fluid Sci. 105 (2019) 247–260.
[27] A. Menezes, A.K.A. de Araújo, J.C. Passos, Horizontal flow boiling of carbon dioxide inside a conventional tube and parallel minichannels of a square cross-section, Int. J. Therm. Sci. 208 (2025) 109388.
[28] Y. Bian, Z. Chen, Z. Li, Y. Liang, Y. Li, X. Lu, D. Yuan, Z. Feng, Experimental investigation on the effects of inclined grooves on flow boiling heat transfer and instability in a minichannel heat sink, Int. J. Heat. Mass Transf. 236 (2025) 126333.
[29] F. Pérez-Flores, C. Treviño, L. Martínez-Suástegui, Transient mixed convection heat transfer for opposing flow from two discrete flush-mounted heaters in a rectangular channel of finite length: effect of buoyancy and inclination angle, Int. J. Therm. Sci. 104 (2016) 357–372.
[30] 3M, 3M Fluorinert Electronic Liquid FC-72 TDS_FINAL.Pdf, (2019).
[31] O. Engineering, Pressure transducers, (2018).
[32] M. Vermaak, D. Orejon, J. Dirker, K. Sefiane, J.P. Meyer, Pressure and thermal characterisation of dynamic instabilities during flow boiling in micro/mini-channels at different Azimuth orientations, Appl. Therm. Eng. 218 (2023) 119292.
[33] M. Vermaak, J. Potgieter, J. Dirker, M.A. Moghimi, P. Valluri, K. Sefiane, J. P. Meyer, Experimental and numerical investigation of micro/mini channel flow-boiling heat transfer with non-uniform circumferential heat fluxes at different rotational orientations, Int. J. Heat. Mass Transf. 158 (2020) 119948.
[34] M.M. Shah, Applicability of correlations for boiling/condensing in macrochannels to minichannels, Heat Mass Transf. Res. J. 2 (2018) 22–32.
[35] J.R. Thome, State-of-the-art overview of boiling and two-phase flows in microchannels, Heat Transf. Eng. 27 (9) (2006) 4–19.
[36] S.S. Mehendale, A.M. Jacobi, R.K. Shah, Fluid flow and heat transfer at micro- and meso-scales with application to heat exchanger design, Appl. Mech. Rev. 53 (7) (2000) 175–193.
[37] H. D, Q.H. Tran, C. Kang, A. Haldar, J. Huh, Effects of ambient temperature and relative humidity on subsurface defect detection in concrete structures by active thermal imaging, Sensors 17 (8) (2017) 1718.
[38] R.P. Madding, Emissivity Measurement and Temperature Correction Accuracy considerations, in: AeroSense '99, SPIE, 1999, p. 9.
[39] P. Vasileiadou, K. Sefiane, T.G. Karayiannis, J.R.E. Christy, Flow boiling of ethanol/water binary mixture in a square mini-channel, Appl. Therm. Eng. 127 (2017) 1617–1626.
[40] Y. Wang, K. Sefiane, Effects of heat flux, vapour quality, channel hydraulic diameter on flow boiling heat transfer in variable aspect ratio micro-channels using transparent heating, Int. J. Heat. Mass Transf. 55 (9–10) (2012) 2235–2243.
[41] J. Barber, D. Brutin, K. Sefiane, J.L. Gardarein, L. Tadrist, Unsteady-state fluctuations analysis during bubble growth in a "rectangular" microchannel, Int. J. Heat. Mass Transf. 54 (23–24) (2011) 4784–4795.
[42] L. Qin, A. Widyatama, N. Zhang, J.C. Passos, K. Sefiane, S. Li, D. Orejon, Addressing the synergistic effect of hydraulic diameter and aspect ratio on experimental flow boiling in microchannels, Appl. Therm. Eng. 274 (2025) 126566.
[43] K. Zhou, C. Coyle, J. Li, J. Buongiorno, W. Li, Flow boiling in vertical narrow microchannels of different surface wettability characteristics, Int. J. Heat. Mass Transf. 109 (2017) 103–114.
[44] C.-N. Huang, C.R. Kharangate, Consolidated model for predicting flow boiling critical heat flux in single-sided and double-sided heated rectangular channels, Int. J. Heat. Mass Transf. 160 (2020) 120132.
[45] C.R. Kharangate, L.E. O'Neill, I. Mudawar, Effects of two-phase inlet quality, mass velocity, flow orientation, and heating perimeter on flow boiling in a rectangular channel: part 1 – Two-phase flow and heat transfer results, Int. J. Heat. Mass Transf. 103 (2016) 1261–1279.
[46] M. Piasecka, Correlations for flow boiling heat transfer in minichannels with various orientations, Int. J. Heat. Mass Transf. 81 (2015) 114–121.
[47] M. Piasecka, Heat transfer mechanism, pressure drop and flow patterns during FC-72 flow boiling in horizontal and vertical minichannels with enhanced walls, Int. J. Heat. Mass Transf. 66 (2013) 472–488.
[48] M. Piasecka, B. Maciejewska, Enhanced heating surface application in a minichannel flow and the use of the FEM and trefftz functions for the solution of inverse heat transfer problem, Exp. Therm. Fluid Sci. 44 (2013) 23–33.
[49] Y. Li, H. Wu, Y. Yao, Enhanced flow boiling heat transfer and suppressed boiling instability in counter-flow stepped microchannels, Int. J. Heat. Mass Transf. 194 (2022) 123025.
[50] K. Luo, W. Li, J. Ma, W. Chang, G. Huang, C. Li, Silicon microchannels flow boiling enhanced via microporous decorated sidewalls, Int. J. Heat. Mass Transf. 191 (2022) 122817.
[51] W. Li, K. Luo, C. Li, Y. Joshi, A remarkable CHF of 345W/cm^2 is achieved in a wicked-microchannel using HFE-7100, Int. J. Heat. Mass Transf. 187 (2022) 122527.
[52] G. Criscuolo, W.B. Markussen, K.E. Meyer, M.R. Kærn, High heat flux flow boiling of R1234yf, R1234ze(E) and R134a in high aspect ratio microchannels, Int. J. Heat. Mass Transf. 186 (2022) 122215.
[53] G.R. Warrier, C.-J. Kim, Y.S. Ju, Microchannel cooling device with perforated side walls: design and modeling, Int. J. Heat. Mass Transf. 68 (2014) 174–183.
[54] R.J. Moffat, Describing the uncertainties in experimental results, Exp. Therm. Fluid Sci. 1 (1) (1988) 3–17.
[55] Y. Wang, K. Sefiane, S. Harmand, Flow boiling in high-aspect ratio mini- and micro-channels with FC-72 and ethanol: experimental results and heat transfer correlation assessments, Exp. Therm. Fluid Sci. 36 (2012) 93–106.
[56] A. Widyatama, G. Duursma, D. Orejon, K. Sefiane, Flow boiling characteristics of HFE-7000 in high aspect ratio microchannels with the effect of flow orientation, Appl. Therm. Eng. 257 (2024) 124094.
[57] B. Kim, An experimental study on fully developed laminar flow and heat transfer in rectangular microchannels, Int. J. Heat Fluid Flow 62 (2016) 224–232.
[58] X.F. Peng, G.P. Peterson, Convective heat transfer and flow friction for water flow in microchannel structures, Int. J. Heat. Mass Transf. 39 (12) (1996) 2599–2608.
[59] P.V.R. Nanda Kishore, S. Venkatachalapathy, P. Kalidoss, Experimental investigation on thermohydraulic performance of hybrid nanofluids in a novel minichannel heat sink, Thermochim. Acta 721 (2023) 179452.
[60] T.M. Harms, M.J. Kazmierczak, F.M. Gerner, Developing convective heat transfer in deep rectangular microchannels, Int. J. Heat Fluid Flow 20 (2) (1999) 149–157.
[61] G.L. Morini, Analytical determination of the temperature distribution and nusselt numbers in rectangular ducts with constant axial heat flux, Int. J. Heat. Mass Transf. 43 (5) (2000) 741–755.
[62] R.K. Shah, A.L. London, Laminar Flow Forced Convection in ducts: a Source Book for Compact Heat Exchanger Analytical Data, Academic press, 2014.
[63] A. Barletta, Fully developed mixed convection and flow reversal in a vertical rectangular duct with uniform wall heat flux, Int. J. Heat. Mass Transf. 45 (3) (2002) 641–654.
[64] J.P. Hartnett, M. Kostic, Heat transfer to Newtonian and non-Newtonian fluids in rectangular ducts, Adv. Heat Transfer (1989) 247–356.
[65] H. Wang, M. Pang, Y. Diao, Y. Zhao, Heat transfer characteristics and flow features of nanofluids in parallel flat minichannels, Powder Technol. 402 (2022) 117321.
[66] P.-S. Lee, S.V. Garimella, D. Liu, Investigation of heat transfer in rectangular microchannels, Int. J. Heat. Mass Transf. 48 (9) (2005) 1688–1704.
[67] M. Ozdemir, M. Mahmoud, T.G. Karayiannis, Flow boiling heat transfer in a rectangular copper microchannel, J. Therm. Eng. 2 (2) (2016) 761–773.
[68] H. Bhowmik, C.P. Tso, K.W. Tou, F.L. Tan, Convection heat transfer from discrete heat sources in a liquid cooled rectangular channel, Appl. Therm. Eng. 25 (16) (2005) 2532–2542.
[69] Y. Sudo, M. Kaminaga, H. Ikawa, Combined forced and free convective heat transfer characteristics in narrow vertical rectangular channel heated from both sides, J. Nucl. Sci. Technol. 24 (5) (1987) 355–364.
[70] D. Barnea, Y. Luninski, Y. Taitel, Flow pattern in horizontal and vertical two phase flow in small diameter pipes, Can. J. Chem. Eng. 61 (5) (1983) 617–620.
[71] S. Ali, G. Jin, Y. Fan, Characterization of gas–Liquid two-phase slug flow using distributed acoustic sensing in horizontal pipes, Sensors 24 (11) (2024) 3402.
[72] L.L. Wang, Study on effect of gas-liquid two phase physical feature on slug flow in microchannels, Front. Phys. 11-2023 (2023).
[73] K.A. Triplett, S.M. Ghiaasiaan, S.I. Abdel-Khalik, D.L. Sadowski, Gas-liquid two-phase flow in microchannels part I: two-phase flow patterns, Int. J. Multiph. Flow 25 (3) (1999) 377–394.
[74] M.E. Rahman, J.A. Weibel, Influence of convective heat transfer and wall thermal capacity on dynamic interactions between wall temperature and pressure drop oscillations during microchannel flow boiling, Int. J. Heat. Mass Transf. 221 (2024) 125111.
[75] M.D. Clark, M.E. Rahman, J.A. Weibel, S.V. Garimella, Effect of thermal capacitance on microchannel heat sink response to pressure drop oscillations, Int. J. Heat. Mass Transf. 214 (2023) 124369.
[76] H. Ye, L.Y.X. Lum, R. Kandasamy, H. Zhao, J.Y. Ho, Flow boiling heat transfer enhancement of R134a in additively manufactured minichannels with microengineered surfaces, Appl. Therm. Eng. 256 (2024) 124150.

[77] S. Ndao, Y. Peles, M.K. Jensen, Experimental investigation of flow boiling heat transfer of jet impingement on smooth and micro structured surfaces, Int. J. Heat. Mass Transf. 55 (19) (2012) 5093–5101.

[78] J. Liu, H. Wu, X. Hua, Z. Liu, Silicon-based microjet array impingement boiling heat transfer with SDS surfactant solutions, Appl. Therm. Eng. 257 (2024) 124454.

[79] K.H. Chang, C. Pan, Two-phase flow instability for boiling in a microchannel heat sink, Int. J. Heat Mass Transf. 50 (11) (2007) 2078–2088.